Development of a Digital Feedback System for Advanced Ion Manipulation Techniques within a Penning Trap

by

Jost Herkenhoff

Bachelor's Thesis

Bremen City University of Applied Sciences

March 2020

Referees: Prof. Dr.-Ing. Mirco Meiners
Prof. Dr. phil. Sören Peik

This bachelor's thesis has been carried out by Jost Herkenhoff at the Max Planck Institute for Nuclear Physics in Heidelberg

Abstract

The high-precision Penning-trap mass spectrometer PENTATRAP aims at measurements of mass ratios of highly charged ions with an uncertainty of a few parts in 10^{-12}. Within the context of this thesis, the development of an active feedback system and its possible applications for the PENTATRAP experiment are described. This system allows to electronically feed back the signal from the axial detection electronics to one or multiple electrodes of the Penning trap, enabling the implementation of advanced ion manipulation techniques. It was successfully used to cool the apparent temperature of the detection electronics below the 4.2 K environment of the trap setup, enabling the application of ion feedback cooling. Furthermore, the quality-factor and the center frequency of the resonator, used in the detection system, was shown to be modified by coupling the feedback signal to the resonator. The feedback system was implemented using a novel concept, making use of real-time digital processing algorithms on an FPGA. This leads to very stable feedback operation and allows for highly dynamic variation of the feedback parameters, opening the possibility for new measurement schemes. A phase-sensitive measurements technique for the axial frequency was successfully implemented and tested, which inherently has the potential to achieve better accuracy compared to the commonly used axial dip detection. Additionally, a single-ion self-excited oscillator was realized, enabling the determination of the axial frequency at very high repetition rates. As the precision of the PENTATRAP experiment is currently mainly limited by the uncertainty of the axial frequency measurement, the feedback system developed in this thesis will directly contribute to improving the precision of the mass measurements.

Zusammenfassung

Das Hochpräzisions-Penningfallen-Massenspektrometer PENTATRAP hat das Ziel die Massenverhältnisse hochgeladener Ionen mit einer relativen Unsicherheit in der Größenordnung 10^{-12} zu messen. In dieser Arbeit werden die Entwicklung eines aktiven Rückkopplungssystems und seine möglichen Anwendungen für das PENTATRAP-Experiment beschrieben. Dieses System ermöglicht die elektronische Rückkopplung des Signals von der axialen Detektionselektronik zu einer oder mehreren Elektroden der Penningfalle, wodurch neuartige Ionenmanipulationstechniken realisiert werden können. Es wurde erfolgreich verwendet um die scheinbare Temperatur der Detektionselektronik unter die 4,2 K-Umgebung des Fallenaufbaus zu kühlen, was unter Anderem das aktive Kühlen von Ionen ermöglicht. Darüber hinaus wurde gezeigt, dass der Qualitätsfaktor und die Resonanzfrequenz des Resonators, welcher im Detektionssystem verwendet wird, durch Koppeln des Rückkopplungssignals an den Resonator modifiziert werden kann. Bei der Entwicklung des Rückkopplungssystems wurde ein neuartiges Konzept verfolgt, bei dem die Signalverarbeitung digital auf einem FPGA implementiert wurde. Die damit erzielte hohe Stabilität der Rückkopplung und die hochdynamische Variierbarkeit der Rückkopplungsparameter ermöglicht die Realisierung neuartiger Messmethoden. Eine Methode für die phasensensitive Messung der Axialfrequenz wurde erfolgreich implementiert und getestet. Die damit potentiell erreichbare Genauigkeit übertrifft die der aktuell verwendeten Axial-Dip Methode. Zusätzlich wurde ein selbsterregter Oszillator mit einem einzelnen Ion realisiert, welcher die Bestimmung der Axialfrequenz mit sehr hohen Wiederholungsraten ermöglicht. Da die Präzision des PENTATRAP-Experiments derzeit hauptsächlich durch die Unsicherheit der Axialfrequenzmessung begrenzt ist, wird das in dieser Arbeit entwickelte Rückkopplungssystem direkt zur Verbesserung der Präzision der Massenmessungen beitragen.

Contents

List of Figures

List of Tables

1

Introduction

The mass of an atom is an important fundamental property in a number of fields of science. Especially in the field of physics, precise mass measurements are of utmost importance for numerous applications: Due to the inherent connection of mass and energy, they can be used to determine the binding energies within the electron shell and the nucleus of an atom. In astrophysics, accurate mass values are required to understand the nucleosynthesis processes that led to the formation of the elements we see today [1]. Furthermore, precise mass measurements can be used to test fundamental theories like quantum electrodynamics (QED) [2, 3] or the CPT theorem (charge, parity and time invariance) [4], and have been used to prove Einstein's mass-energy relationship $E = mc^2$ to hold to a level of at least 0.00004% [5, 6]. The required relative precision of the mass measurements depends on the physics being investigated. In Tab. 1.1, a general comparison of the required accuracy for different fields of science is outlined.
The most precise mass spectrometry methods rely on the measurement of the revolution frequency of an ion inside a magnetic field [7]. Nowadays, Penning traps are the most suitable devices based on this method, offering high-precision mass measurements of ions or charged particles with relative uncertainties down to 10^{-11} or lower [8, 9, 10].
The Penning-trap experiment Pentatrap, located at the Max Planck Institute for Nuclear Physics, is designed for high-precision mass measurements of highly charged ions within the medium-heavy to heavy mass range [11]. With an aimed relative mass uncertainty of a few parts in 10^{-12}, Pentatrap will contribute to the determination of an upper limit for the neutrino mass [12, 13, 14], entering the domain of physics beyond the Standard Model, and to test QED in the regime of extreme electric fields [15]. In

Table 1.1: Comparison of the required relative mass uncertainties for various fields of science [12].

Field of science	Mass uncertainty $\frac{\delta m}{m}$
Chemistry	$\leq 10^{-5}$
Nuclear structure physics	$\leq 10^{-6}$
Astrophysics	$\leq 10^{-7}$
Weak interaction studies	$\leq 10^{-8}$
Fundamental constants	$\leq 10^{-9}$
CPT tests	$\leq 10^{-10}$
QED in highly charged ions	$\leq 10^{-11}$
Neutrino physics	$\leq 10^{-11}$

order to reach such low uncertainties, the motional state of the ion within the Penning trap must be extremely well controlled. This is typically achieved by irradiating an RF (radio frequency) field into the Penning trap, allowing a certain degree of control over the ion motion. Currently, the accuracy of PENTATRAP is mainly limited by the frequency determination uncertainty of the axial ion motion.
In the scope of this thesis, an electronic feedback system was developed, opening up the possibility for more advanced ion manipulation techniques like feedback cooling, self-excited oscillation and damping reduction. The feedback system was implemented using real-time digital signal processing on an FPGA. This enabled the implementation of a phase-sensitive detection technique for the determination of the axial ion frequency, inherently offering higher frequency precision compared to the previously used technique.
The next chapter, chapter 2, gives an introduction to the physical background of Penning-trap experiments, focusing on a description of the ion motion and its detection within a Penning trap. Furthermore, this chapter introduces a mathematical description of active feedback in the context of Penning-trap physics. The experimental setup of PENTATRAP is outlined in chapter 3. In chapter 4, the realization of the active feedback system is presented, starting with an overview of the system architecture and then giving a more in-depth description of the hardware and FPGA implementation. Afterwards, chapter 5 introduces the new phase sensitive technique for the determination of the axial frequency at PENTATRAP. Chapter 6 presents the results of various characterization measurements of the feedback system in connection with the PENTATRAP experiment. Furthermore, the first measurements of the new axial measurement technique and the results of a single ion self-excited oscillator are presented. Finally, chapter 7 gives a summery and a short outlook.

2

Penning Trap Physics

An ideal way to study the properties of atoms or subatomic particles is to spatially confine them to a finite volume for an extended period of time [12]. In the case of charged particles or ions, this can be achieved using the interaction between the particle and a surrounding electromagnetic field. However, as Samuel Earnshaw stated in 1842, it is not possible to fully confine a charged particle in all three spatial dimensions solely by means of a static electric or a static magnetic field [16]. Penning traps overcome this limitation by using a superposition of a magnetic and electric field. Today, Penning traps are widely used, among other things, for high-precision mass measurements [17], measurements of magnetic moments [12], and quantum computation [18].

This chapter will focus on the basic principles of ion storage inside Penning traps and introduces the image-charge detection technique. Additionally, the concept of active feedback for ion manipulation is introduced by devising a mathematical description and analyzing its implication on the ion motion. This chapter will cover the necessary knowledge required to follow this thesis, focusing on the ideal Penning trap. Any effects that might arise from unavoidable imperfections in the experimental setup will not be covered here (an extensive introduction to Penning trap physics can be found in [19]).

2.1 Ion motion in a Penning trap

A homogeneous magnetic field $\vec{B} = B_0\vec{e}_z$ along the z-direction will force an ion with velocity $\vec{v}$ and charge q onto a circular orbit perpendicular to the magnetic-field axis due to the Lorentz force $\vec{F} = q(\vec{v} \times \vec{B})$. The revolution frequency of this motion, called the *free cyclotron frequency*, is given by

$$\omega_c = \frac{q}{m} B_0 \,, \tag{2.1}$$

with $\frac{q}{m}$ being the charge-to-mass ratio of the ion. However, a homogeneous magnetic field alone is not sufficient to fully confine the ion, since it is still able to move freely in the direction of the magnetic field lines (axial direction). In order to prevent it from drifting out of the trap, an electrostatic quadrupole field of the form

$$\vec{E} = C_2 U_0 \begin{pmatrix} x \\ y \\ -2z \end{pmatrix} \tag{2.2}$$

is superimposed, creating a harmonic potential well in the axial direction with its minimum at $z = 0$. The coefficient C_2 is a geometrical constant that can be determined from the electrode structure of the Penning trap [19, 20], while U_0 denotes the trapping potential. Figure 2.1 shows two possible electrode structures commonly used to create the electrostatic quadrupole field.

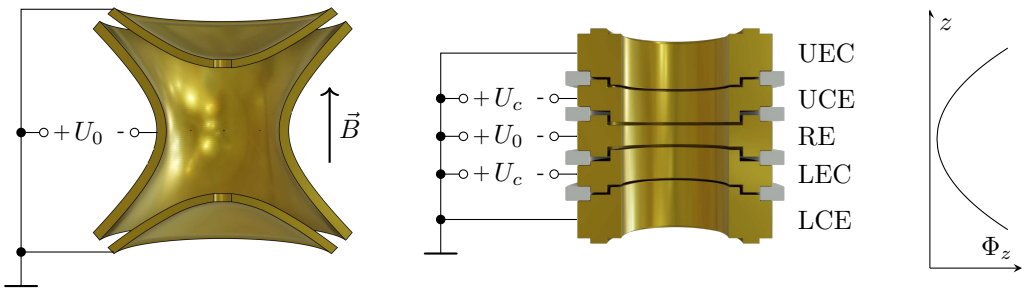

Figure 2.1: Drawing of a hyperbolical (a) and cylindrical (b) Penning trap and a qualitative representation (c) of their axial electric potential $\Phi_z = \int E_z$. The electrodes of the hyperbolical trap resemble the equipotential surface of the electric potential. The cylindrical trap, which can usually be machined to higher precision, uses a set of five electrodes[a] and a correction voltage U_c to approximate the ideal trap potential.
[a] Upper/lower end cap (UEC, LEC); Upper/lower correction electrode (UCE, LCE); Ring electrode (RE)

The divergence of the electrostatic field in the x-y plane, as shown in Eq. (2.2), exerts a force on the ion in the azimuthal direction, leading to a slight modification of its radial circular motion. A complete description of the motion of a single ion in a Penning trap can be derived by evaluating the Lorentz force $\vec{F} = q(\vec{E} + \vec{v} \times \vec{B})$ acting on the ion. Applying Newton's second law $\vec{F} = m\vec{a}$, with $\vec{a}$ being the acceleration of the ion, results in the following system of differential equations:

$$\begin{pmatrix} \ddot{x} \\ \ddot{y} \\ \ddot{z} \end{pmatrix} = \frac{qC_2U_0}{m} \begin{pmatrix} x \\ y \\ -2z \end{pmatrix} + \frac{qB_0}{m} \begin{pmatrix} \dot{y} \\ -\dot{x} \\ 0 \end{pmatrix} . \tag{2.3}$$

It can be seen, that the differential equation for the axial motion (z component) describes a simple harmonic oscillation with the eigenfrequency

$$\omega_z = \sqrt{\frac{2qC_2U_0}{m}} . \tag{2.4}$$

The x- and y-components of the ion's motion are described by two coupled differential equations, that can be solved by introducing the complex variable $u = x + jy$ and using an exponential ansatz $u = e^{j\omega t}$. Their solutions are then specified by two independent harmonic oscillations with the eigenfrequencies

$$\omega_+ = \frac{\omega_c}{2} + \sqrt{\frac{\omega_c^2}{4} - \frac{\omega_z^2}{2}} \qquad \text{and} \tag{2.5}$$

$$\omega_- = \frac{\omega_c}{2} - \sqrt{\frac{\omega_c^2}{4} - \frac{\omega_z^2}{2}} , \tag{2.6}$$

which are called the modified cyclotron (ω_+) and the magnetron frequency (ω_-), respectively. It can be seen, that certain choices of parameters can lead to complex frequencies, resulting in an unstable ion motion. By demanding the equations (2.5) and (2.6) to have real roots, the following stability criterion can be derived:

$$\omega_c > \sqrt{2}\omega_z , \tag{2.7}$$

or equivalently

$$\frac{q}{m}B_0 > 2\sqrt{\frac{qC_2U_0}{m}} . \tag{2.8}$$

In order for this criterion to hold true, the radial confinement due to the magnetic field must be stronger than the defocusing of the electrostatic field. This can be achieved by employing a strong magnetic field and a weak electrostatic potential. This gives rise to the typical hierarchy of frequencies in a Penning trap:

$$\omega_c > \omega_+ \gg \omega_z \gg \omega_- . \tag{2.9}$$

For the PENTATRAP experiment ($B_0 \approx 7\,\mathrm{T}$, $U_0 = -50\,\mathrm{V}$, $C_2 = -1.5 \cdot 10^{-2} \frac{1}{\mathrm{mm}^2}$), exemplary eigenfrequencies for a $^{187}\mathrm{Re}^{30+}$ ion are

$$\nu_+ = 173\,\mathrm{MHz}\,, \quad \nu_z = 768\,\mathrm{kHz}\,, \quad \text{and} \quad \nu_- = 17\,\mathrm{kHz}\,. \tag{2.10}$$

The superposition of all three eigenmotions describing the trajectory of the ion is depicted in Fig. 2.2.
It must be noted, that the free cyclotron frequency ω_c, initially introduced in Eq. (2.1), is no longer an eigenfrequency of the trapped ion, due to the presence of the electrostatic field. However, by combining equations (2.4) to (2.6), the relation

$$\omega_c = \sqrt{\omega_+^2 + \omega_-^2 + \omega_z^2} \tag{2.11}$$

for calculating the free cyclotron frequency can be derived, which is known as the Brown-Gabrielse-Invariance theorem [19]. It is particularly useful for high-precision measurements, as it holds true even if certain imperfections are present in the experimental setup (e.g. not perfectly aligned $\vec{E}$ and $\vec{B}$ fields).

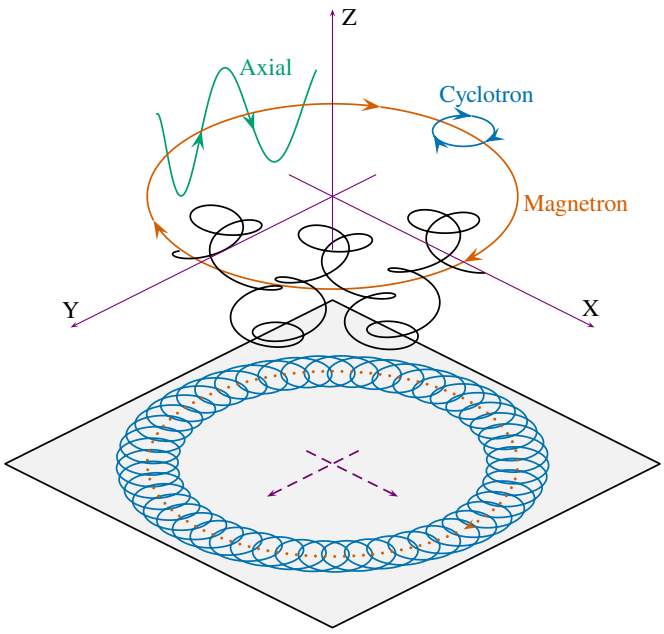

Figure 2.2: Trajectory of a single ion in a Penning trap. The black line represents the full motion of the ion, constructed by the superposition of the individual eigenmotions, shown in green, blue and orange. Additionally, the projection of the combined radial modes onto the x-y plane is shown (blue line).

2.2 Mass measurements in Penning traps

By determining the free cyclotron frequency ω_c of an ion with known charge state q, its mass can be easily calculated using Eq. (2.1), provided that the magnetic field strength B_0 is known. However, the precision to which the magnetic field strength can be measured is usually not sufficient for the precision that is aimed for in Penning-trap mass measurements. Therefore, typically only relative mass ratios between two different ions are performed by determining their respective free cyclotron frequencies within the same trap. When calculating their relative mass ratio $\frac{m_1}{m_2}$ by rearranging Eq. (2.1) it can be seen that the magnetic field strength B_0 is cancelled out.
Using the invariance theorem (Eq. (2.11)) to calculate the free cyclotron frequency results in an uncertainty of

$$\Delta\omega_c = \sqrt{\Big(\underbrace{\frac{\omega_+}{\omega_c}}_{\approx 1}\Delta\omega_+\Big)^2 + \Big(\underbrace{\frac{\omega_z}{\omega_c}}_{\approx 10^{-2}}\Delta\omega_z\Big)^2 + \Big(\underbrace{\frac{\omega_-}{\omega_c}}_{\approx 10^{-3}}\Delta\omega_-\Big)^2}, \tag{2.12}$$

where $\Delta\omega_+$, $\Delta\omega_-$ and $\Delta\omega_z$ represent the uncertainties of the respective eigenfrequency measurements. When considering the typical hierarchy of the eigenfrequencies shown in Eq. (2.9), it can be seen that the individual uncertainty contributions are weighted differently. The annotations shown in Eq. (2.12) provide a rough estimate for the orders of magnitude of typical eigenfrequency ratios [21].

2.3 Manipulation of the eigenmotions

The motional state of a confined ion can be controlled by irradiating an RF (radio frequency) field into the Penning trap. This is typically achieved by applying an RF signal directly to one of the trap electrodes. The following sections will outline the two most commonly used excitation schemes.

2.3.1 Dipolar excitation

By applying an RF field with a frequency at or near a specific eigenfrequency and its field vector pointing in the direction of the associated eigenmotion, the oscillatory amplitude can be excited to a higher state. For an excitation of the axial mode, the RF field must be applied to an end-cap or correction electrode. For an excitation of the radial modes, a laterally split electrode must be used.
Increasing the amplitude of an eigenmotion can be useful during the ion preparation phase before the actual measurement, in order to be more easily detectable (see section 2.4). Furthermore, it is commonly used during phase-sensitive detection techniques, which will be introduced in section 2.4.4, to imprint a well-known phase on one of the eigenmotions.

2.3.2 Quadrupolar excitation

Applying an RF excitation to a quarter of a split electrode produces a field that extends in the axial as well as the radial direction, resulting in a quadrupolar excitation at the position of the ion. By applying a frequency at the sum or difference of two eigenfrequencies, a coupling between the respective modes can be achieved, leading to an energy transfer between one oscillatory motion to another. For the duration of the quadrupolar excitation, the energy is periodically transferred back and forth between the modes at a rate of exactly half the Rabi frequency Ω_0 [22, 11]. In the context of Penning-trap experiments, it is defined by

$$\Omega_0 = \frac{q}{m}\frac{E_0}{2}\frac{1}{\sqrt{\omega_z\omega_\pm}}\,, \tag{2.13}$$

with E_0 being the excitation field strength at the position of the ion. Quadrupolar excitation is commonly used to couple one of the radial motions to the axial mode, which often is the only mode that can be detected directly (see section 2.4).

2.4 Ion detection

In the following section a non-destructive detection technique, called *Fourier Transform Ion cyclotron resonance* [23] (FT-ICR), is introduced.

2.4.1 Image current

The Shockley-Ramo theorem [24, 25] states, that a moving point charge q induces an image current i_{ind} in a nearby electrode. When considering two infinitely extended parallel plates separated by the distance D, a moving ion with velocity $\vec{v}$ placed inside the gap will induce the image current

$$i_{\text{ind}}(t) = \frac{q}{D}\,\vec{n}\cdot\vec{v}(t)\,, \tag{2.14}$$

with $\vec{n}$ denoting the normal vector of the plates. If the ion performs harmonic oscillations orthogonal to the plates with amplitude Z_0 and frequency ω_z, the induced current becomes

$$i_{\text{ind}}(t) = \frac{q\omega_z}{D}Z_0\sin(\omega_z t)\,. \tag{2.15}$$

The infinite plate model can be applied to the Penning trap by modeling its electrode structure as an effective plate distance D_{eff}. In [26], an analytical expression for D_{eff} is derived for the special case of a cylindrical Penning trap. As the image current induced by the ion's motion is typically in the order of 10 fA [11], a transimpedance conversion with a large impedance Z_{det} is used within the detection system to convert it into a measurable voltage $u_{\text{det}}(t) = i_{\text{ind}}(t)\,Z_{\text{det}}$. Typically, this impedance is realized by connecting a superconducting coil with inductance L to the pickup electrode, forming a resonant tank circuit together with the parasitic trap capacitance C. The unavoidable

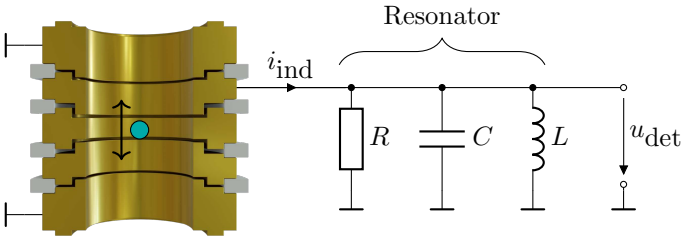

Figure 2.3: Schematic diagram of the axial detection principle. The dashed components (R and C) model parasitic effects.

ohmic and dielectric losses within the detection system can be modeled as a lumped resistor R, as it is shown in Fig. 2.3. A common measure for the losses within a resonant circuit is the *quality factor* (Q-factor) [27], defined as

$$Q = R\sqrt{\frac{C}{L}} = \frac{R}{\omega_{\text{res}} L}\,. \tag{2.16}$$

The frequency $\omega_{\text{res}} = \frac{1}{\sqrt{LC}}$, called the resonance frequency of the resonator, is defined as the frequency at which the imaginary terms in its impedance

$$Z_{\text{det}} = \left[\frac{1}{R} - \frac{j}{\omega L} + j\omega C\right]^{-1} = R\left[1 + j\,Q\left(\frac{\omega}{\omega_{\text{res}}} - \frac{\omega_{\text{res}}}{\omega}\right)\right]^{-1} \tag{2.17}$$

exactly cancel out, leaving only the real valued impedance $Z_{\text{det}}(\omega_{\text{res}}) = R$. At this point the impedance reaches its global maximum, leading to the highest possible signal strength of u_{det}. This can be achieved by varying the trap potential and therefore, according to Eq. (2.4), adjusting the axial frequency until it exactly lines up with the resonance frequency of the resonator.

2.4.2 Interaction of the ion with the detection system

While the voltage drop u_{det} across the resonator allows to detect the axial motion of the ion, it also produces an additional electric field inside the trap, exerting a counteracting force

$$F = -\frac{q}{D_{\text{eff}}}\,u_{\text{det}} = -\frac{q^2\,Z_{\text{det}}}{D_{\text{eff}}^2}\,\dot{z} \tag{2.18}$$

on the ion. Inserting this into the axial equation of motion, presented in Eq. (2.3), results in the new differential equation

$$\ddot{z} + \underbrace{\frac{q^2\,Z_{\text{det}}}{D_{\text{eff}}^2\,m}}_{\Gamma}\,\dot{z} + \omega_z^2 z = 0\,, \tag{2.19}$$

which resembles the differential equation of a linearly damped harmonic oscillator with the complex damping term Γ. It can be solved using the ansatz $z = z_0\, e^{\lambda t}$, with

$$\lambda = -\frac{\Gamma}{2} + j\omega_z \sqrt{1 - \frac{\Gamma^2}{4\omega_z^2}}\,. \tag{2.20}$$

As the contribution of the $\Gamma^2/4\omega_z^2$ term is insignificant [28], it will be neglected in the following discussion, resulting in the simplified form

$$\lambda \approx j\omega_z - \frac{\Gamma}{2}\,. \tag{2.21}$$

By using the fact, that the imaginary and real part of λ represent the frequency and the damping of the ion's oscillation, two interesting implications of the interaction between the ion and the detection system can be found:

Resistive cooling: The real part of λ leads to a damping of the ion's oscillation amplitude. During this process, energy from the axial mode gets transferred into the resonant circuit, which is typically connected to a heat bath at liquid helium temperatures (4.2 K). The temperature associated with the ion's motion decays exponentially with the time constant

$$\tau = \frac{1}{2\mathrm{Re}\{\Gamma\}} \approx \frac{m D_{\mathrm{eff}}^2}{q^2 \mathrm{Re}\{Z_{\mathrm{res}}(\omega_z)\}}\,, \tag{2.22}$$

until it is in thermal equilibrium with the resonator. At this point, the retroacting electric field exerting the damping force on the ion is dominated by the Johnson-Nyquist noise [29, 30] of the resonator. The ion is now effectively driven by the incoherent thermal noise of the resonator, leading to no further decrease of the amplitude. This process is commonly referred to as *resistive cooling* [31].

Frequency pulling: If the axial frequency of the ion is not exactly aligned with the resonance frequency of the resonator, it experiences an additional frequency shift due to the non-zero imaginary part of the complex damping term Γ. This effect, called *frequency pulling*, can be calculated using

$$\tilde{\omega}_z = \mathrm{Im}\{\lambda\} \approx \omega_z - \mathrm{Im}\left\{\frac{\Gamma}{2}\right\} = \omega_z - \frac{q^2\, \mathrm{Im}\{Z_{\mathrm{det}}(\omega_z)\}}{2 D_{\mathrm{eff}}^2\, m}\,. \tag{2.23}$$

The frequency $\tilde{\omega}_z$ denotes the shifted frequency, while ω_z is the unperturbed axial frequency as introduced in Eq. (2.4).
Figure 2.4 shows the effect of frequency pulling for different detunings of the axial frequency. It can be seen, that the frequency shift can be minimized by tuning the ion's axial frequency to exacly match the resonance frequency of the resonator or by deliberately choosing a sufficiently large frequency detuning.

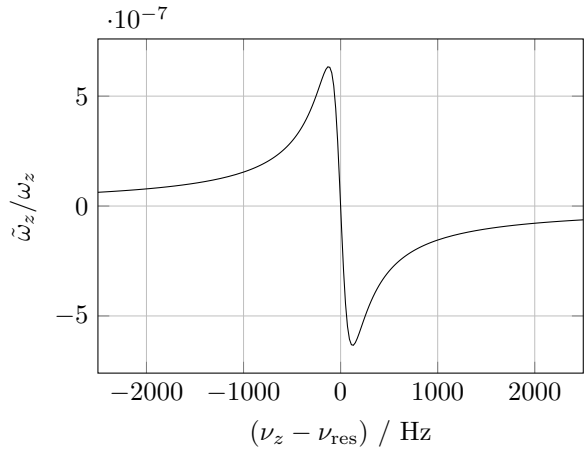

Figure 2.4: Frequency pulling induced by the interaction of the ion with the detection system as a function of detuning of the axial frequency from the resonance frequency of the resonator.

2.4.3 Dip spectrum

If the ion's axial mode is in thermal equilibrium with the resonator, its properties can be modeled as an equivalent series LC circuit[32] with the parameters

$$L_{\text{ion}} = \frac{mD_{\text{eff}}^2}{q^2}\,, \tag{2.24a}$$

$$C_{\text{ion}} = \frac{q^2}{m\omega_z^2 D_{\text{eff}}^2}\,. \tag{2.24b}$$

In Fig. 2.5a the complete equivalent circuit of an ion coupled to a resonator is shown. Considering that an ideal series LC circuit at its resonance frequency acts as an electrical short, it can be seen that the impedance of the complete circuit must rapidly drop to zero when approaching ω_z. This characteristic of the coupled system manifests itself as a *dip* in the spectral power density of the thermal noise of the resonator, which can be detected by analyzing the signal in the frequency domain (Fig. 2.5b). By fitting the resulting spectrum with an appropriate physical model, the axial frequency of the ion can be determined.

Double-dip

The previously described *single-dip technique* is typically solely used to directly detect the axial eigenmode. However, by coupling one of the radial modes to the axial mode, as introduced in section 2.3, this technique can be extended to indirectly measure the magnetron and modified cyclotron frequency.
The coupling allows energy to be transferred from the radial motions to the axial motion, where it will be dissipated due to resistive cooling (described in section 2.4.2).

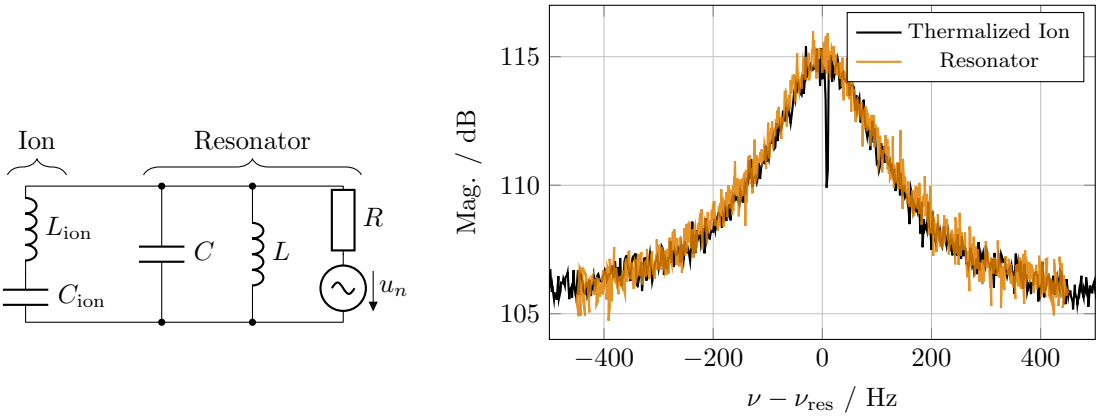

(a) **(b)**

Figure 2.5: The schematic diagram in (a) represents the equivalent circuit model for an ion coupled to the resonator. The Johnson-Nyquist noise of R is modeled by an equivalent voltage source u_n. A measured noise spectrum of a real resonator is depicted in (b) without an ion (orange) and with an ion in thermal equilibrium with the resonator (black).

Eventually, the radial mode will reach thermal equilibrium with the resonator, at which point the Rabi oscillation of the mode-coupling essentially acts like an amplitude modulation. As a result, the axial dip spectrum splits into two dips at the frequencies

$$\omega_{l,r} = \omega_z \pm \frac{\Omega_0}{2}\,, \tag{2.25}$$

separated by the Rabi frequency Ω_0 introduced in Eq. (2.13). By measuring the frequencies of the two dips, the real radial frequencies can be calculated using the relations

$$\omega_+ = \omega_l + \omega_r - \omega_z + \omega_{\text{rf}}\,, \tag{2.26a}$$

$$\omega_- = -\omega_l - \omega_r - \omega_z + \omega_{\text{rf}}\,, \tag{2.26b}$$

where ω_{rf} denotes the excitation frequency used for mode coupling. The double-dip technique allows the measurement of all three eigenfrequencies by only using an axial detection system.

The dip / double-dip measurement scheme has the advantage of being able to measure the frequency of a specific mode at its lowest possible energy level, minimizing systematic errors due to trap anharmonicities or relativistic shifts [33]. However, since the measured signal is made up entirely of incoherent noise, the signal-to-noise ratio only increases with $\sqrt{t}$ over the measurement time t, making this measurement scheme a slow process (for PENTATRAP $20\,\text{s} < t < 1\,\text{min}$). Moreover, the accuracy of the frequency estimation can only be as good as the physical model that is used for fitting.

2.4.4 Phase-sensitive detection of the radial frequencies

As shown in section 2.2, the uncertainty of the modified cyclotron frequency has the largest contribution to the total uncertainty of the mass measurement, making it desirable to reduce this uncertainty as much as possible. For a more precise measurement of the modified cyclotron frequency than with the double-dip method, a phase-sensitive technique called *Pulse and Phase* (PnP) [34] is commonly used. It can be described as a three step process:

1. **Phase imprint:** The (initially cold) cyclotron motion is excited to a comparably high amplitude with a well-defined initial phase $\phi(t_0)$ by applying a dipolar excitation pulse.

2. **Phase evolution:** By allowing the cyclotron motion to evolve freely for a precisely known time t_{evol}, the instantaneous phase accumulates linearly with

$$\phi(t_{\mathrm{evol}}) = \omega_+ \cdot (t_{\mathrm{evol}} - t_0) + \phi(t_0)\,. \tag{2.27}$$

3. **Phase readout:** By applying a qudrupolar excitation pulse of the length $t_\pi = \frac{\pi}{2\Omega_0}$ (called a π-*pulse* [34]), the entire amplitude and the phase of the cyclotron motion can be phase-coherently transferred to the axial mode at once, where it can be measured using the axial detection system.
   After that, by knowing the phase at t_0 and t_{evol}, the modified cyclotron frequency can be calculated using

$$\omega_+ = \frac{\phi(t_{\mathrm{evol}}) - \phi(t_0)}{t_{\mathrm{evol}} - t_0} = \frac{\Delta\phi}{\Delta t}\,. \tag{2.28}$$

One complication in this technique arises from the fact that phases can only be measured modulo 2π. To overcome this issue, the phase difference $\Delta\phi$ must be interpreted as an integer multiple of 2π and a residual phase $\Delta\varphi \in [0, 2\pi)$:

$$\Delta\phi = 2\pi N + \Delta\varphi\,. \tag{2.29}$$

While $\Delta\varphi$ is the phase difference that is measured, the integer N, representing the number of completed cycles during t_{evol}, can not be uniquely determined from a single measurement. However, by doing multiple PnP cycles with different phase evolution times, N can be determined in a process called *phase unwrapping* [21].

2.5 Active feedback

The application of active feedback within the context of Penning-trap physics opens the possibility to either directly or indirectly alter certain characteristics of the ion's eigenmotions. There are two scenarios of active feedback that can be distinguished, namely *resonator feedback* and *direct ion feedback*, which will be discussed in the following sections.

2.5.1 Resonator feedback

By capacitively coupling the feedback signal back to the resonator, its characteristics can be modified. Figure (2.6a) shows the circuit diagram of the resonator with applied feedback. The amplifier, labeled with G, models the feedback path as a complex gain factor $G = G_0 e^{j\phi}$, with G_0 being the absolute gain and ϕ being the phase shift within the feedback path. The Johnson-Nyquist noise of the resonator at temperature T is modeled as a current source with a power spectral density [29, 30] of

$$\overline{i_n^2} = \frac{4\,k_B\,T}{R}\,, \tag{2.30}$$

where k_B is the Boltzmann constant. In order to understand the effect of active feedback on the resonator's characteristics, an analytical description for the admittance Y of the shown circuit can be derived using complex phasor arithmetic. The voltage $U_{C_{\mathrm{fb}}}$ and the feedback current I_{fb} can be expressed by

$$U_{C_{\mathrm{fb}}} = U - UG = U(1-G)\,, \tag{2.31}$$

$$I_{\mathrm{fb}} = U_{C_{\mathrm{fb}}}\,Y_{C_{\mathrm{fb}}} = U(1-G)\,j\omega C_{\mathrm{fb}}\,, \tag{2.32}$$

with $Y_{C_{\mathrm{fb}}} = j\omega C_{\mathrm{fb}}$ being the admittance of the feedback capacitance at frequency ω. With this, an admittance

$$\tilde{Y}_{\mathrm{fb}} \coloneqq \frac{I_{\mathrm{fb}}}{U} = (1-G)\,Y_{C_{\mathrm{fb}}} = (1-G)\,j\omega C_{\mathrm{fb}} \tag{2.33}$$

can be defined which equivalently models the complete feedback path as a self-contained lumped element parallel to the RLC circuit, as shown in Fig. 2.6b: The total admittance of the circuit as seen by the noise current source can therefore be written as

$$\begin{aligned} Y &= Y_R + Y_C + Y_L + \tilde{Y}_{\mathrm{fb}}\,, \\ &= \frac{1}{R} + j\omega C - \frac{j}{\omega L} + (1-G)j\omega C_{\mathrm{fb}}\,. \end{aligned} \tag{2.34}$$

Further analysis of this expression reveals two interesting implications of the active feedback:

Resonance frequency shift

As the resonance frequency of a parallel RLC circuit is defined as the frequency at which the imaginary part equals zero, an expression for the resonance frequency ω_{res} of the resonator can be derived. By extracting the imaginary part of Eq. (2.34)

$$\mathrm{Im}\{Y\} = \omega C - \frac{1}{\omega L} + \omega C_{\mathrm{fb}}(1 - \mathrm{Re}\{G\})\,, \tag{2.35}$$

and demanding $\mathrm{Im}\{\,Y|_{\omega=\omega_0}\,\} = 0$, the resonance frequency can be found to be

$$\omega_{\mathrm{res}} = \frac{1}{\sqrt{LC + LC_{\mathrm{fb}}(1 - \mathrm{Re}\,\{G\})}}\,. \tag{2.36}$$

As this result shows, the resonance frequency can be freely altered by applying in-phase feedback ($\mathrm{Re}\{G\} \neq 0$). This frequency shift is shown in Fig. 2.7 as a function of feedback gain and phase.

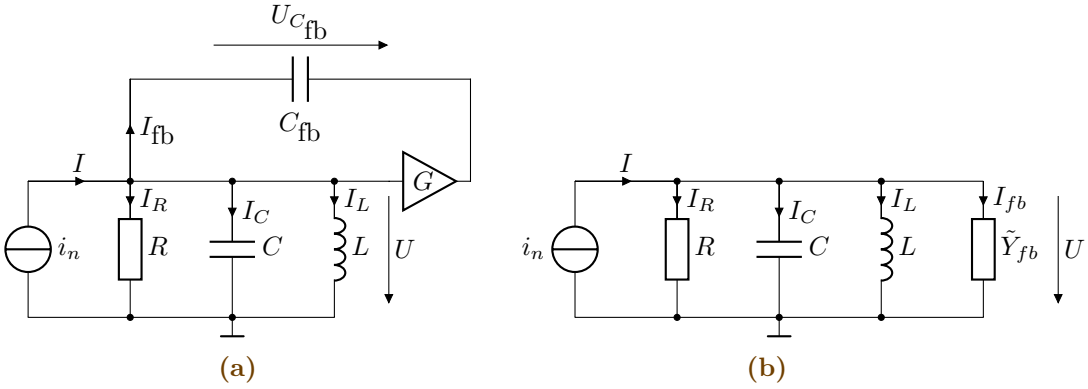

Figure 2.6: The circuit diagram (a) shows the resonator of the detection system with applied feedback. The coupling capacitance C_{fb} and the amplification $G = G_0 e^{j\phi}$, representing the phase shift ϕ and gain G_0 of the feedback system, can be modeled by an equivalent admittance $\tilde{Y}_{\mathrm{fb}}$, as it's shown in figure (b).

Temperature and damping control

By extracting the real part of the admittance Y,

$$\mathrm{Re}\{Y\} = \frac{1}{R} + \mathrm{Im}\{G\}\omega C_{\mathrm{fb}}\,, \tag{2.37}$$

the concept of an effective resistance of the resonator with active feedback, defined as

$$R_{\mathrm{eff}} := \frac{1}{\mathrm{Re}\{Y\}} = \frac{R}{1 + \omega C_{\mathrm{fb}} R\,\mathrm{Im}\{G\}}\,, \tag{2.38}$$

can be introduced. Applying this to Eq. (2.30), a corresponding effective temperature [35, 36] of the resonator can be derived:

$$T_{\mathrm{eff}} = T\,\frac{R_{\mathrm{eff}}}{R} = \frac{T}{1 + \omega C_{\mathrm{fb}} R\,\mathrm{Im}\{G\}}\,. \tag{2.39}$$

This allows to resistively cool ions to lower temperatures than the actual temperature T of the resonator (usually 4.2 K) by tuning the feedback so that $\mathrm{Im}\{G\} > 0$ (e.g. 90° phase shift). However, the minimal temperature that can be achieved using this technique is limited by the additional noise introduced within the feedback path. A detailed analysis of the minimal achievable temperature is discussed in [35].

Contrastingly, by applying feedback with $\mathrm{Im}\{G\} < 0$ (e.g. −90° phase shift), the effective resistance of the resonator can be increased, theoretically leading to arbitrarily high signal-to-noise ratios. However, as $\mathrm{Im}\{G\}$ tends towards $\frac{1}{\omega C_{\mathrm{fb}} R}$, the damping of the resonator eventually becomes so small or even negative, that any random noise fluctuation can lead to undamped oscillations of the resonator.

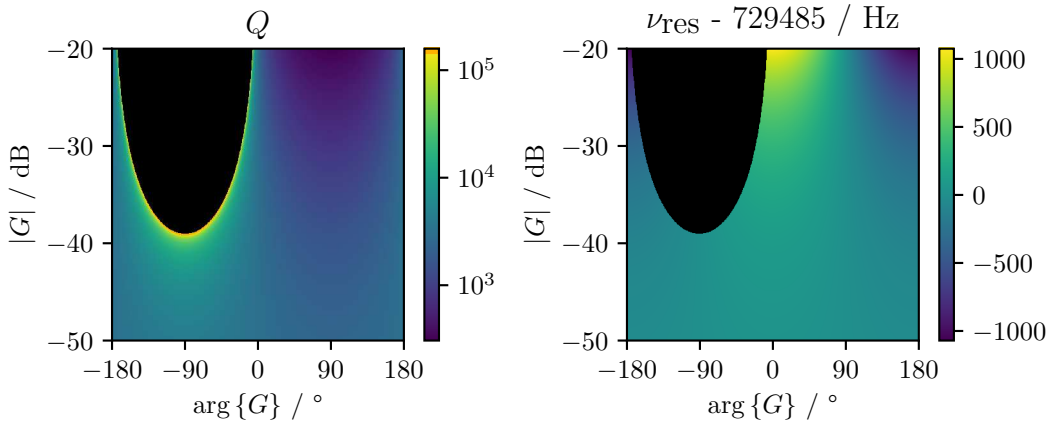

Figure 2.7: Theoretical evaluation of the Q-factor and resonance frequency of a resonator[a] with active feedback. The black areas mark the instability regions (free oscillation of resonator).
[a] $R = 19.5\,\mathrm{M\Omega}$, $C = 33\,\mathrm{pF}$, $L = 1.4\,\mathrm{mH}$, $C_{\mathrm{fb}} = 20\,\mathrm{fF}$

Q-Factor
The previously described effects can be combined to derive a new expression for the Q-factor as a function of feedback gain:

$$Q = \frac{R_{\mathrm{eff}}(\omega_{\mathrm{res}})}{\omega_{\mathrm{res}}\, L} = \frac{R\sqrt{C + C_{\mathrm{fb}}(1 - \mathrm{Re}\,\{G\})}}{\sqrt{L}\,(1 + \omega C_{\mathrm{fb}} R\,\mathrm{Im}\{G\})}\,. \tag{2.40}$$

In Fig. 2.7, the variation of the Q-factor is depicted for different feedback gains and phases.

2.5.2 Ion feedback

Applying the feedback signal directly to an electrode of the Penning trap will superimpose an additional electric field within the trap, directly influencing the motion of the ion. Analogous to Eq. (2.18), the force exerted on the ion due to this new field can be written as

$$F_{\mathrm{fb}} = \frac{q}{D_{\mathrm{eff,fb}}} u_{\mathrm{fb}}\,, \tag{2.41}$$

with $D_{\mathrm{eff,fb}}$ being the effective plate distance for the feedback electrode, as described in section 2.4.1. As the feedback voltage u_{fb} is directly derived from the output u_{det} of the detection system, it can be written as

$$u_{\mathrm{fb}} = u_{\mathrm{det}}\, G = G\,\frac{q\, Z_{\mathrm{det}}}{D_{\mathrm{eff}}}\dot{z}\,. \tag{2.42}$$

The factor G is a complex constant modeling the phase shift and gain of the feedback path. Inserting Eq. (2.42) into (2.41) results in the feedback force

$$F_{\mathrm{fb}} = G\,\frac{q^2\, Z_{\mathrm{det}}}{D_{\mathrm{eff}}\, D_{\mathrm{eff,fb}}}\dot{z}\,. \tag{2.43}$$

Incorporating this into the equation of motion of the ion in interaction with the detection system (Eq. (2.19)) results in the new equation of motion

$$\ddot{z} + \underbrace{\frac{q^2\, Z_{\mathrm{det}}}{D_{\mathrm{eff}}^2\, m}}_{\Gamma} \dot{z} - G\, \frac{q^2\, Z_{\mathrm{det}}}{m\, D_{\mathrm{eff}}\, D_{\mathrm{eff,fb}}} \dot{z} + \omega_z^2 z = 0\,,$$

$$\ddot{z} + \underbrace{\frac{q^2\, Z_{\mathrm{det}}}{m\, D_{\mathrm{eff}}^2}}_{\Gamma} \left(1 - G \frac{D_{\mathrm{eff}}}{D_{\mathrm{eff,fb}}}\right) \dot{z} + \omega_z^2 z = 0\,. \tag{2.44}$$

This reveals that the original damping term Γ can be artificially altered by the active feedback. As it was previously shown in section 2.4.2, this new complex damping term can be used to calculate the modified damping constant and cooling time constant

$$\gamma_{\mathrm{fb}} = \gamma \left(1 - \mathrm{Re}\{G\} \frac{D_{\mathrm{eff}}}{D_{\mathrm{eff,fb}}}\right)\,, \tag{2.45a}$$

$$\tau_{\mathrm{fb}} = \frac{1}{\gamma_{\mathrm{fb}}} = \tau \frac{1}{1 - \mathrm{Re}\{G\} \frac{D_{\mathrm{eff}}}{D_{\mathrm{eff,fb}}}}\,, \tag{2.45b}$$

for the ion with active feedback, with γ and τ being the damping constant and cooling time constant of the ion without feedback, respectively. Likewise, the new axial frequency can be calculated using

$$\tilde{\omega}_{z,\mathrm{fb}} = \omega_z - \mathrm{Im}\{\Gamma\} \left(1 - \mathrm{Im}\{G\} \frac{D_{\mathrm{eff}}}{D_{\mathrm{eff,fb}}}\right)\,. \tag{2.46}$$

Figure 2.8 shows the damping constant and the detuning of the axial frequency for different feedback gain and phase settings.

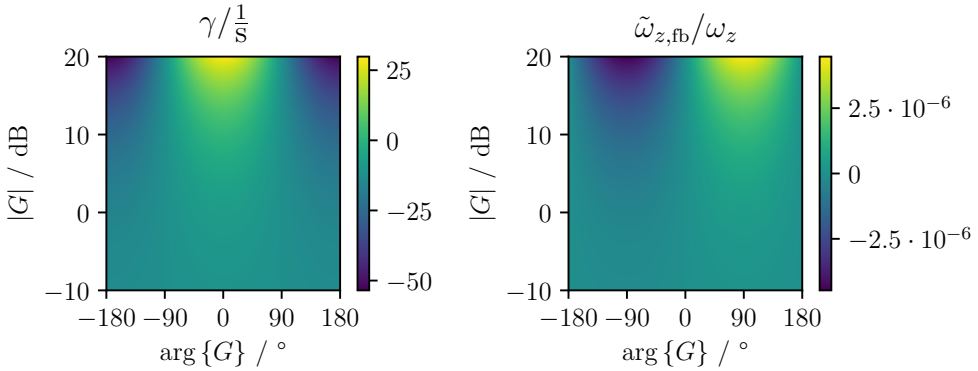

Figure 2.8: Theoretical evaluation of the damping factor and frequency shift of an ion with active feedback. ($R = 19.5\,\mathrm{M\Omega}$, $C = 33\,\mathrm{pF}$, $L = 1.4\,\mathrm{mH}$, $U_0 = -46.667\,\mathrm{V}$, $C_2 = -1.5 \cdot 10^{-2}\,\mathrm{m}^{-2}$, $D_{\mathrm{eff}} = 11.1\,\mathrm{mm}$, $D_{\mathrm{eff,\,fb}} = 31.5\,\mathrm{mm}$, $q/m = 30e/186.2u$)

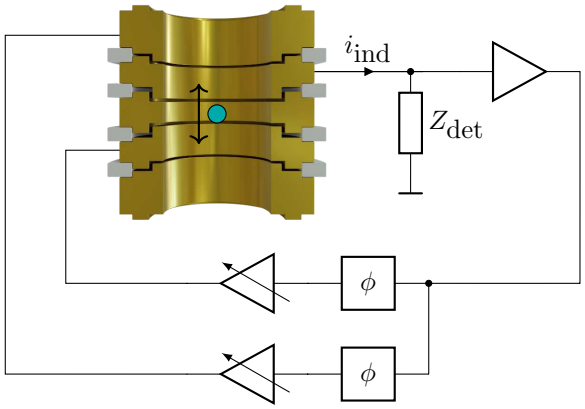

Figure 2.9: Schematic diagram of a Penning trap with active feedback using two separate feedback paths, enabling the cancellation of signal feedthrough to the resonator

2.5.3 Resonator feedthrough cancellation

When applying feedback to a trap electrode, a certain part of this signal will be coupled directly back into the resonator due to parasitic capacitive coupling to the pickup-electrode of the detection system. This effect will be called *resonator feedthrough* within the context of this thesis. While this effect can be utilized to implement resonator feedback (as described in section 2.5.1), it's certainly not desired when aiming for pure ion feedback. To overcome this issue, a second, independent feedback path is attached to another trap electrode, as shown in Fig. 2.9. By carefully tuning the phase shift and gain ratios of the two paths, a complete cancellation of the resonator feedthrough can be accomplished. As the image-current detection principle requires the pickup electrode to be axially offset from the ion's center of motion, the ion will still experience the feedback force.

3

The Pentatrap Experiment

The Penning-trap experiment Pentatrap is designed for high-precision mass measurements of highly charged ions (HCI), aiming at an accuracy of a few parts in 10^{-12}. Its multi-trap configuration, consisting of five individual Penning traps, makes it unique compared to other Penning-trap experiments. Pentatrap is located in the experimental hall of the Max Planck Institute for Nuclear Physics and spans two floors: the ion production takes place on the ground-floor while the actual Penning-trap setup is located in a temperature stabilized room in the basement.
This chapter briefly outlines the most important parts of the Pentatrap experiment, including the production and transportation of the ions (section 3.1), the magnet and Penning-trap setup (sections 3.2 to 3.3) and the detection electronics (section 3.4).

3.1 Ion production and transport

HCIs can be efficiently produced in electron-beam ion traps (EBIT) using the process of electron impact ionization [37]. The Pentatrap experiment features two EBITs for ion production: the commercial DreEBIT [38], which was used to produce the ions for the measurements presented in chapter 6, and the recently commissioned Tip-EBIT [39], specialized for the production of ions of rare species. The DreEBIT is able to produce bare nuclei up to $Z = 30$ and helium- or neon-like charge states for heavier elements up to uranium [40].
The HCIs are transported to the Penning-trap setup within a beamline consisting of several ion-optical lenses as shown in Fig. 3.1. The complete beamline, as well as the

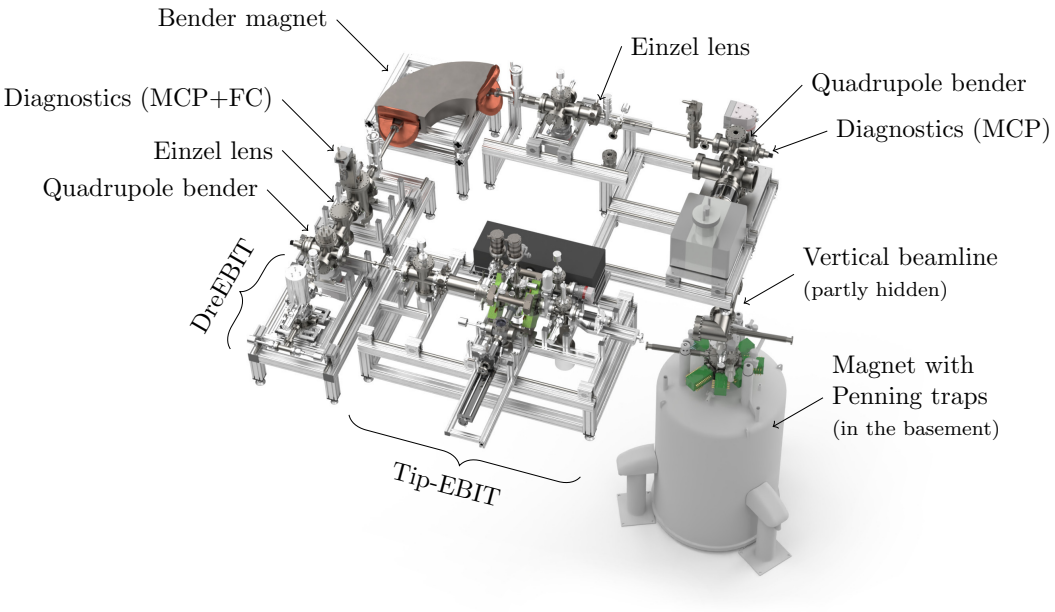

Figure 3.1: CAD model of the PENTATRAP experiment, including the ion sources DreEBIT and Tip-EBIT, the beamline and the magnet in the basement. For details see text.

Penning-trap setup, is pumped down to ultra-high vacuum to allow for an efficient transport and a long lifetime of the stored ions. A bender magnet is used to select ions with specific charge-to-mass $\frac{q}{m}$ ratios from the ion beam. As the actual Penning-trap setup is situated in the basement below the beamline, the ions are bend downwards using a quadrupole bender. In the following vertical beamline, the ions are decelerated using pulsed drift-tubes, after which they are finally ready to be confined within the Penning traps. Further information on the ion production and transport is presented in [41].

3.2 Magnet

The homogeneous magnetic field needed to confine the ions within the Penning traps is produced by a commercial 7 T magnet. The magnet is cooled to superconducting temperatures using a combination of liquid nitrogen and helium. The level and pressure within the helium reservoir is actively stabilized in order to achieve a high temporal magnetic field stability [42]. A vertical bore within the magnet allows the insertion of a cryogenic assembly (shown in Fig. 3.2), housing the Penning traps itself as well as the detection electronics. As the cryogenic assembly is thermally connected to the liquid helium bath of the magnet, the inner surfaces of its vacuum chamber provide a means of cryogenic pumping, resulting in an ultra-high vacuum of better than 10^{-13} mbar [15]. This allows for a trapping time of several days for ions with up to 30+ charge state [21].

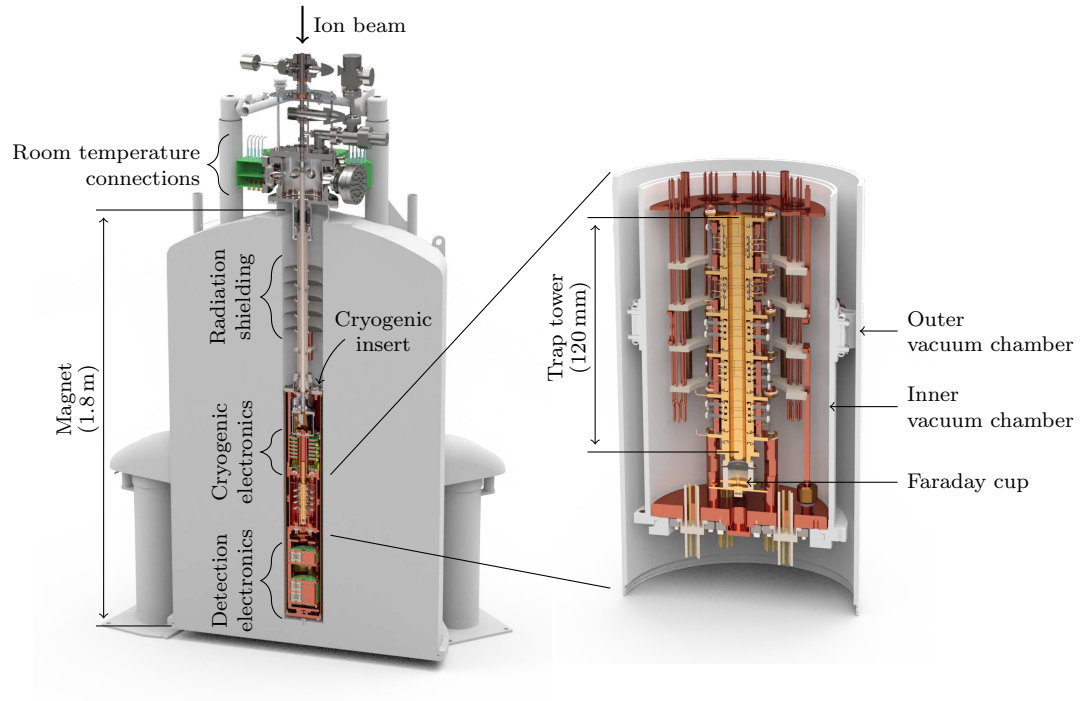

Figure 3.2: **Left:** Cross section of the 7 T magnet (simplified) with the cryogenic insert of the PENTATRAP experiment. **Right:** Detailed view of the trap-tower assembly, consisting of five individual Penning traps.

3.3 Trap tower

The heart of PENTATRAP is the trap tower consisting of five individual cylindrical Penning traps. The usage of multiple traps in close proximity to each other opens up the possibility for sophisticated measurement procedures [15], e.g. the simultaneous measurement of two ion species in adjacent traps. As all five traps are designed to be identical, they share the same geometrical and electrical properties listed in Tab. 3.1.

Table 3.1: Geometrical and electrical parameters of a single Penning trap of the PENTATRAP experiment. The electrostatic coefficient C_2 and the effective electrode distance D_{eff} are simulated values, while the electrode capacitance C_{trap} is measured [43].

C_2	D_{eff}		C_{trap}	
	EC	CE	EC	CE
$-1.496(7) \cdot 10^{-2} \frac{1}{\text{mm}^2}$	31.5 mm	11.1 mm	13 pF	13 pF

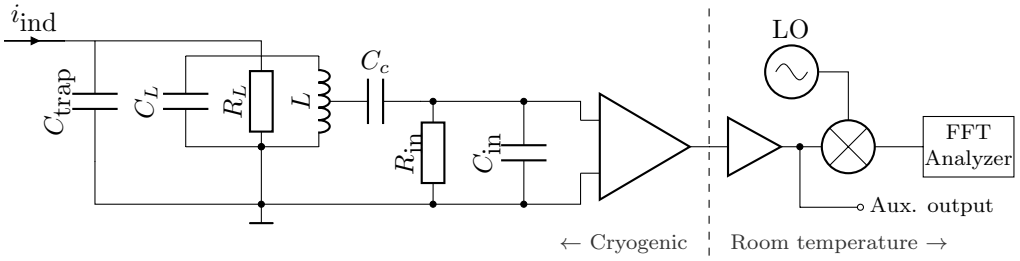

Figure 3.3: Schematic diagram of the complete axial detection system including its parasitic effects.

3.4 Detection electronics

The electronics used for ion detection can be divided into a cryogenic and a room temperature part, as shown in Fig. 3.3. The cryogenic electronics part is encapsulated within a copper housing directly underneath the trap tower and is cooled to liquid helium temperatures. It comprises the superconducting coils, used to form the resonant circuit described in section 2.4.1, as well as a set of low-noise amplifiers. The amplified signal is guided out of the cryogenic assembly, where it is further amplified and then downmixed to $\approx 20\,\text{kHz}$, in order to be easily digitizable using the FFT analyzer [41]. Besides that, an auxiliary output provides access to the non-downmixed signal, which will be utilized for the realization of the feedback system explained in chapter 4.
The current version of PENTATRAP is only equipped with detection systems for the traps 2 and 3. Their parameters are listed in Tab. 3.2. While the other traps can still be used for ion storage, it is not possible to detect ions there.
Further information on the detection electronics is presented in [11].

Table 3.2: Measured parameters of the detection electronics for trap 2 and 3, respectively [21, 44, 43]. L and C_L are the inductance and parasitic capacitance, of the resonator coil. The "tap" value denotes the winding ratio at which the tap of the resonator coil, as seen in Fig. 3.3, is placed.

trap	L	C_L	C_c	C_{in}	tap	ν_{res}	Q
2	1.4 mH	10 pF	10 nF	2.1 pF	1/3	740 kHz	4400
3	3.3 mH	6.9 pF	10 nF	2.1 pF	1/3	504 kHz	6800

4

Realization of an Active Feedback System

In section 2.5, the mathematical description of active feedback in the context of Penning-trap experiments was introduced, showing that it enables a completely new set of ion-manipulation techniques. Within this thesis, an active feedback system for the Pentatrap experiment was developed, assembled and integrated into the experimental setup. A novel concept was pursued, in which the main part of the system is implemented using real-time digital signal processing.
The following chapter addresses the development of the digital feedback system, starting in section 4.1 with a discussion of the design requirements and an outline of the overall system design. A detailed description of the developed hardware and FPGA implementation is presented in section 4.3 and 4.5, respectively. Finally, section 4.7 covers the integration of the feedback system into the Pentatrap experiment.

4.1 Requirements and system level design

As a basic requirement, the feedback system must provide two feedback paths derived from a common input signal with independently adjustable phase shifts and amplification factors. The phase shifts needs to be adjustable within the full range of $0° \leq \phi < 360°$ with rather high resolution of at least 0.1°, while also being very stable with respect to time. These requirements arise partly from the fact, that the application of 0° or 180° feedback to the resonator, used to shift the resonance frequency, gets increasingly sensitive to small phase variations when using high feedback gains (as can be seen in Fig. 2.7). Likewise, when using direct ion feedback, the phase shift of the second feedback path used for resonator feedthrough cancellation must be precisely adjusted in order for both signals to fully cancel out at the resonator (see Section 2.5.3). The new measurement technique, introduced in chapter 5, requires the feedback parameters (gain and phase shift) to be highly dynamically variable with fast response time.
These requirements, especially the variable phase shift within the full 360° range, are hard to meet using conventional analog electronics. Furthermore, the dynamic variation of feedback parameters would require a complex circuit design, likely ending up in a rather specialized and inflexible design. Instead, a novel concept based on digital signal processing was pursued, which is easily capable to fulfill the requirements. For that, the analog input signal, coming from the axial detection system, is first converted into the digital domain, where it can be processed using real-time signal processing algorithms implemented on a field-programmable gate array (FPGA). The FPGA generates two output data-streams for the individual feedback paths, which are finally converted back into analog signals. The data conversion and signal processing is performed using the *Red-Pitaya* platform, which is further described in section 4.2. Additionally, a complete data acquisition system was implemented into the FPGA, enabling the realization of complex control loops as it is needed for the single-ion self-excited oscillator described in section 4.6.1.
The advantages and disadvantages of this digital concept compared to an analog implementation are listed below:

Advantages:

- Not influenced by environmental parameters, such as temperature fluctuations, making it extremely stable with respect to time.
- Possibility for highly dynamic variation of feedback parameters with fast response times.
- High flexibility, as the feedback behavior can be freely modified at any time, without having to make hardware modifications.
- Fully deterministic behavior: For a given starting condition, the same input signal will always produce the same output signal. This enables the system to be fully simulated a priori, resulting in a clear understanding of its characteristics.
- Direct acquisition of the digitized signal possible.

Potential disadvantages:

- Data conversion and processing latencies lead to a non-zero group delay of the system. This introduces a linear frequency dependency to the phase response and thus limits the effective bandwidth of the feedback system or can even lead to instabilities [45].
- Finite bandwidth due to time discrete processing.
- Introduction of quantization noise and round-off errors due to finite word length.

However, the previously listed disadvantages can be overcome or neglected due to the following reasons:

- As the ion and the detection system already represent a very narrow bandwidth system (a few 100 Hz), the feedback bandwidth requirements are not particularly high. Nevertheless, it's still preferable to minimize the constant group delay as much as possible.
- By utilizing analog-to-digital and digital-to-analog converters (ADC and DAC, respectively) with high enough sampling rates, their bandwidth limitation will not pose a problem, as will be further explained in section 4.2.
- The quantization noise introduced within the ADC and DAC can be minimized by appropriately scaling the input and output signals in order to utilize their full dynamic conversion range. To achieve this, additional analog frontends in the form of amplification or attenuation stages have been integrated into the feedback system, as will be explained in section 4.3.

Therefore, the advantages of the digital feedback system outweigh its disadvantages, making it the preferable choice for this use case.

4.2 Red-Pitaya

The *Red-Pitaya STEMLab* (in this thesis referred to as *Red-Pitaya*) is a single-board computer with high speed analog input and output support and extensive real-time processing capabilities [46]. At its heart, it comprises a Xilinx Zynq SoC (System on Chip), combining a dual core ARM A9 CPU with FPGA logic on the same device [47]. The tight coupling between CPU and FPGA provides a high bandwidth interface, which is beneficial for the implementation of the digital acquisition system, outlined in section 4.5.2.
The Red-Pitaya is equipped with a dual channel ADC and DAC, providing a resolution of 14 bits for each channel. Their digital datapaths are directly interfaced to the FPGA logic, offering the real-time processing capabilities needed for the implementation of the feedback system. Both the ADC and DAC provide a sampling frequency of up to 125 MHz, resulting in an oversampling factor of ≈169 for the expected axial frequency of around 740 kHz (trap 2 of PENTATRAP).

As described in section 4.1, the group delay of the data conversion should be minimized in order to achieve the best performance. The pipelined architecture of the ADC introduces a latency of 6 cycles [48] (48 ns), while the DAC can be assumed to have a worst case latency (settling time) of 43 ns [49]. The combined latency results in a group delay of $\tau_g = 91\,\text{ns}$ and therefore in a frequency dependent phase response of

$$\frac{\mathrm{d}\phi}{\mathrm{d}\nu} = -\tau_g\, 360 \approx \frac{33^\circ}{\text{MHz}}\,. \tag{4.1}$$

It must be noted, that this only represents the lowest limit of the achievable group delay and other delays within the analog frontend and the digital processing must also be taken into account.
In addition to the fast analog inputs and outputs, the Red-Pitaya provides a set of four slow (100 kHz) analog outputs which are used to control the variable gain amplifiers within the feedback system (see section 4.3).
The dual core CPU of the Red-Pitaya runs the GNU/Linux operating system, making it possible to realize sophisticated data analysis and control algorithms. The network stack of the Linux operating system in conjunction with the ethernet port of the Red-Pitaya allows the implementation of remote control functionality and to transfer measurement data over the network. The software implementation of the feedback system will be further described in section 4.6.

4.3 Hardware design

Although the main functionality of the feedback system is implemented digitally on the FPGA, a small set of additional hardware is required to achieve the best performance and to fulfill the requirements listed in section 4.1. An overview of the designed hardware is shown in Fig. 4.1.
In order to utilize the full dynamic range of the ADC and DAC, additional analog frontends in the form of input amplifiers and output attenuators are required, being described in section 4.3.1 and 4.3.2, respectively. The analog circuitry is powered using a combination of DC-DC converters and linear regulars, as described in section 4.3.5. In order for the feedback system to achieve the highest possible phase stability, it is designed to operate with an external 10 MHz reference clock. For that, additional clock conditioning and frequency synthesis circuitry, further described in section 4.3.3, is provided. A dedicated trigger input, described in section 4.3.4, opens the possibility to dynamically adjust certain feedback parameters with precise timing.

4.3.1 Input stage

Although the detected axial ion signal has already passed through the cryogenic and room temperature amplifier before entering the feedback system (see section 3.4), its amplitude of a few millivolt is still too small to be acquired by the Red-Pitaya with reasonable resolution. Therefore, further amplification is applied within the input stage

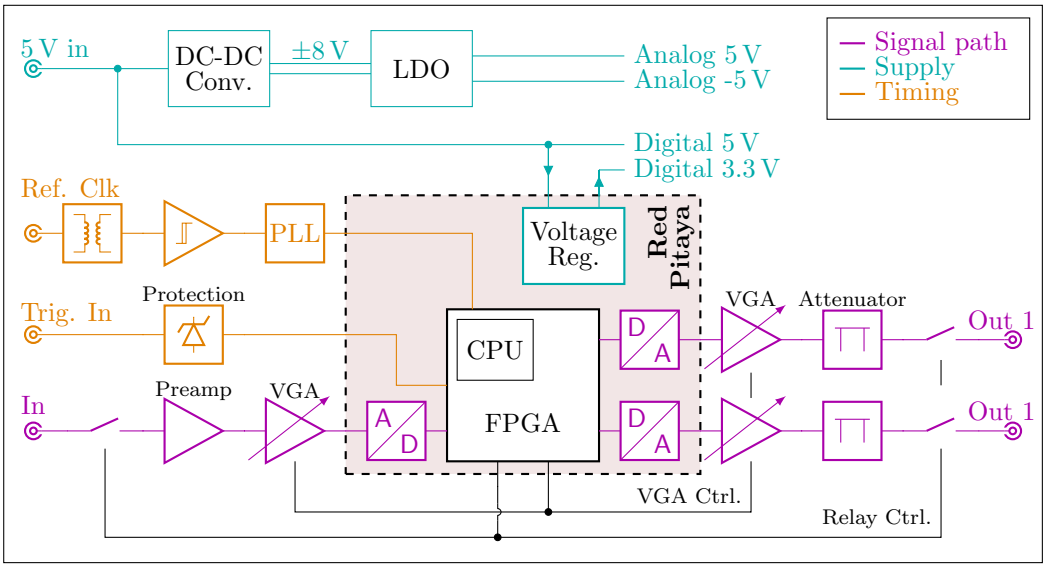

Figure 4.1: Block diagram of the feedback system hardware. For details see text.

of the feedback system, aiming for a final amplitude slightly lower than the Red-Pitaya's input range of ±1 V. At this point, the highest possible dynamic range of the analog-to-digital conversion is achieved.
As depicted in Fig. 4.1, the input signal is initially preamplified using a low-noise instrumentation amplifier (AD8429) configured for a fixed gain of 20 dB, followed by a second stage amplifier (AD8336) with a variable gain of −14 dB to 46 dB. This variable-gain amplifier (VGA) enables the feedback system to accommodate for a large range of input amplitudes, while maintaining the highest possible dynamic range of the analog to digital conversion. It's gain is set using a differential analog voltage in the range of ≈ ±0.5 V [50], which is generated by the slow analog outputs of the Red-Pitaya.
The input signal can be disconnected from the input circuitry using a relay (represented as a simple switch in Fig. 4.1), in order to prevent any potential noise sources within the feedback system from coupling back into the PENTATRAP experiment when the active feedback is not in use.

4.3.2 Output stage

The outputs of the Red-Pitaya's dual channel DAC are connected to an analog output stage featuring two identical signal paths, leading to *Out 1* and *Out 2* in Fig. 4.1. Each path consists of a VGA (AD8336) to accommodate for a large range of output amplitude requirements. The amplification of the VGAs are independently controlled using the slow analog outputs of the Red-Pitaya. Additionally, a set of four fixed π-attenuators with 2 dB, 4 dB, 8 dB and 16 dB can be independently inserted into each output signal path using jumper connectors. The two output signals of the output stage can be independently disabled using two relays.

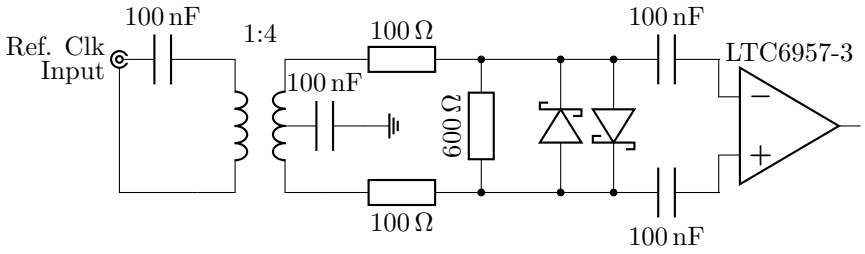

Figure 4.2: Schematic diagram of the reference clock input stage. The input transformer provides galvanic isolation and amplifies the amplitude of the reference clock by a factor of four. The following resistors and diodes provide input protection. The LTC6957-3 converts the signal into CMOS logic level.

4.3.3 Reference clock section

Any fluctuations of the Red-Pitaya's clock frequency will directly influence the signal propagation delay within the digital signal processing, leading to a fluctuating phase shift. Therefore, a stable clock frequency is desired in order to fulfill the phase-stability requirements mentioned in section 4.1. Furthermore, when the acquisition system of the FPGA (see section 4.5.2) is used for frequency determination of the axial ion signal, an accurately known sampling frequency is required.
For this reason, the feedback system is designed to be synchronized to an external 10 MHz reference clock (Ref. Clk in Fig. 4.1), offering a higher stability than the Red-Pitaya's internal clock source. Specifically, the central 10 MHz clock of the PENTATRAP experiment will be used, which is generated by a FS725 rubidium frequency standard, outputting a sine wave with a root-mean-square amplitude of 0.5 V [51].
The reference clock input stage, shown in Fig. 4.2, conditions the incoming clock signal for further processing and provides a certain degree of input protection. The design was taken from [52]. An input transformer amplifies the amplitude of the incoming signal by a factor equal to it's winding ratio ($\frac{N_1}{N_2} = 1:4$), resulting in steeper flanks and therefore leading to a reduction of phase noise in the later stages. It also provides galvanic isolation, reducing the risk of introducing ground loops into the PENTATRAP experiment. When considering the impedance transformation introduced by the transformer, it can be seen that the sum of the three resistors result in a 50 Ω termination on the input:

$$\frac{Z_{\text{prim}}}{Z_{\text{sec}}} = \left(\frac{N_1}{N_2}\right)^2 \quad \rightarrow \quad Z_{\text{prim}} = Z_{\text{sec}} \left(\frac{N_1}{N_2}\right)^2 = 800\,\Omega \left(\frac{1}{4}\right)^2 = 50\,\Omega \tag{4.2}$$

The two antiparallel Shottky diodes in conjunction with the two 100 Ω series resistors provide overvoltage protection. The resulting signal is ac-coupled into an LTC6957 clock buffer, which is specifically designed to convert an analog sine-wave input, as it is provided by the FS725 frequency standard, into CMOS logic levels with low additive phase noise.

The digital output signal of the clock buffer is directly fed into a frequency synthesizer to generate the 125 MHz clock required by the Red-Pitaya. It consists of an AD9552 phase-locked loop (PLL) which is configured for an upconversion ratio of 2:25. The AD9552 permanently checks for the presence of an external reference clock and will automatically fall back to a 10 MHz quartz crystal oscillator if none is detected. This way, the feedback system can be used as a standalone device under degraded timing accuracy.

4.3.4 Trigger input

The APnP measurement technique described in chapter 5 requires the feedback parameters to by dynamically varied with precisely known timing. For this purpose, the feedback system features an external trigger input, which is directly routed to an FPGA input, as seen in Fig. 4.1. Depending on the configuration of the FPGA, this trigger input can serve multiple purposes. In the FPGA implementation described in section 4.5, it is used to enable or disable the feedback operation.
The trigger input circuitry consists of a 50 Ω termination resistor, followed by a 1 kΩ series resistor and two clamping diodes, providing overvoltage protection for the FPGA input. Due to unavoidable signal propagation delays, the latency between asserting the trigger pulse and the corresponding reaction of the feedback system is not zero. For the APnP measurement procedure, this latency will cancel out, as long as it stays constant in between individual trigger events. However, as the trigger events do not necessarily occur synchronized to the FPGA clock, the trigger latency might jitter by up to one clock period (80 ns for the 125 MHz clock frequency). This is avoided in the experimental setup, by synchronizing the trigger pulse generator with the pulse-per-second (PPS) output of the reference clock source, which is also used to derive the FPGA clock. A residual jitter of < 1 ps [53] might arise from the frequency jitter of the PLL that is used to generate the FPGA clock from the reference clock. Although the implication of this residual jitter has not been studied thoroughly yet, it is assumed to be negligible.

4.3.5 Power regulation

The circuitries described in the previous sections have different requirements regarding their supply voltage and their noise sensitivity, as listed in Tab. 4.1. Figure 4.3 outlines the general concept of the power supply architecture. The feedback system is powered using an external 5 V power supply, which is directly used to power the Red-Pitaya as well as the input/output relays and a cooling fan. The Red-Pitaya features an onboard 3.3 V DC-DC converter to supply its internal logic, and is also used to power the reference clock section of the feedback system. It is rated to supply a maximum current of 500 mA, which is sufficient for the components of the reference clock section (see Tab. 4.1). As the high clock frequencies within clock buffer and the PLL can produce significant switching noise, a lot of effort was put into separating the digital supply rails from the analog frontend circuitry.
The analog frontends require a bipolar ±5 V supply rail with very low noise. For that, the single 5 V input of the external power supply is first split into an intermediate bipolar

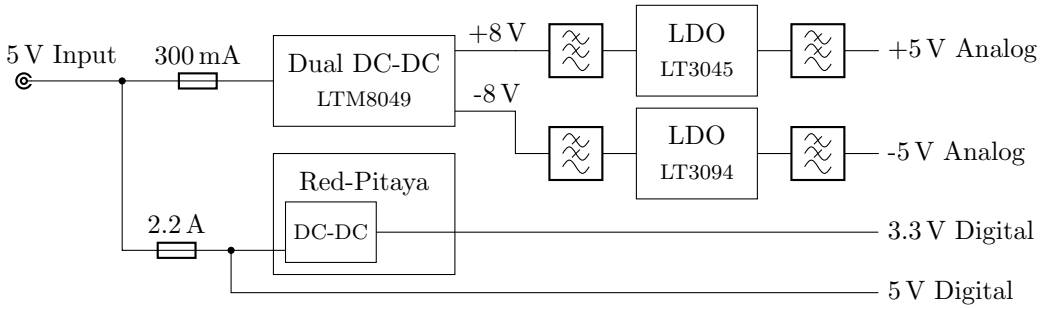

Figure 4.3: Block diagram of the power supply architecture used to power the different parts of the feedback system.

±8 V rail using a dual channel switch-mode converter (LTM8049). A combination of large capacitors, series inductors and ferrite beads were used to filter out the relatively high voltage ripple of the switch-mode converter. In order to minimize switching noise in the frequency range of interest of roughly 100 kHz to 1 MHz, the operating frequency of the LTM8049 was configured to be 1.7 MHz. The filtered intermediate voltage is subsequently further regulated to the final ±5 V analog voltage using two ultra-low noise LDO regulators (LT3045 and LT3094) with additional filtering on their outputs. The intermediate voltage of 8 V was chosen to operate the LDO regulators at their highest PSRR (power supply ripple rejection) rating, which happens to occur at a dropout voltage of ≈ 3 V [54, 55].

4.4 PCB design

The previously described hardware design was implemented on a four-layer PCB (printed circuit board), presented in Fig. 4.4. One of the inner layers was dedicated for a full coverage ground plane, while the second inner layer was exclusively used for supply

Table 4.1: Power supply requirements of the different devices of the feedback system hardware. The listed current values represent the approximated maximum load current of the individual devices. Additionally, a qualitative estimate of the individual devices regarding their sensitivity to external noise and the amount of internally generated noise is listed.

			Noise	
Supply rail	Devices	Current	Sensitivity	Internal
5 V Digital	Red-Pitaya	2 A	Low	High
	Relays, Fan	160 mA	Low	Medium
3.3 V Digital	Ref. clock section	190 mA	Medium	High
±5 V Analog	Analog frontends	140 mA	High	Low

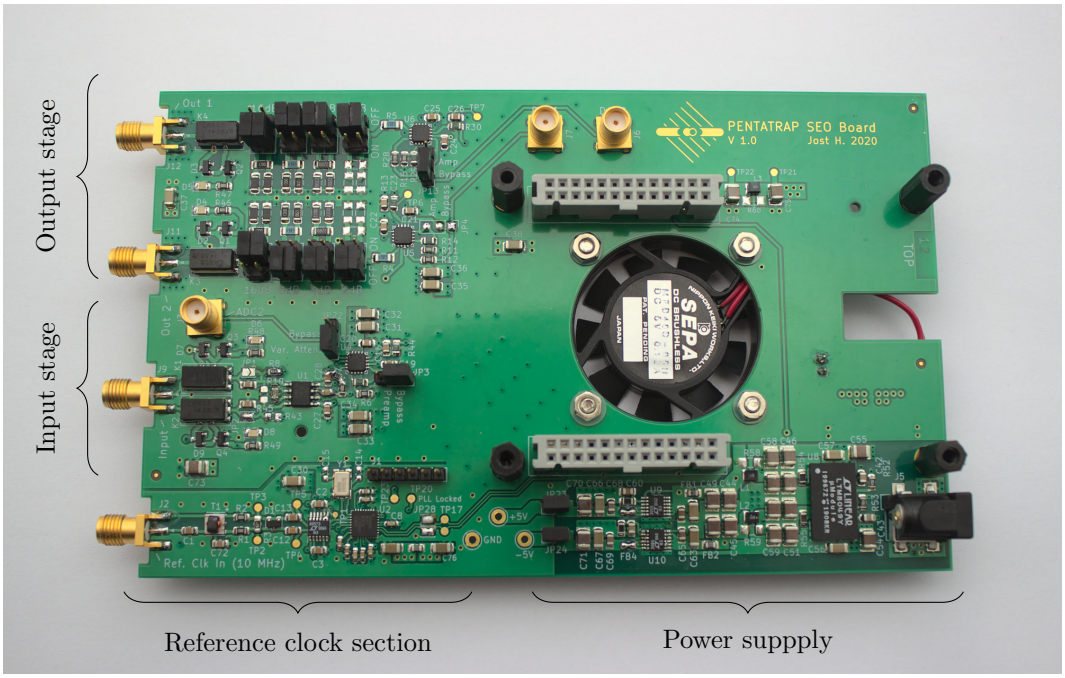

Figure 4.4: Picture of the fully populated PCB.

routing (see Figures B.1 to B.4 in the appendix). In order to minimize the noise in the analog frontends, particular attention was paid to the separation of the digital and analog signal and supply traces. The PCB was designed to fit into a particular aluminium enclosure (see Fig. 4.5b) and was therefore fixed to outline dimensions of 160 mm × 100 mm. As the part count and complexity of the design is not particularly high, this area constraint did not pose a problem.

The PCB is designed to accommodate the Red-Pitaya by stacking them together in a "backpack" configuration, while using the Red-Pitaya's extension connectors as a board-to-board interconnect (see Fig. 4.5a). As the Red-Pitaya's analog input and output signals are not routed through the extension connector, they had to be connected to the PCB using separate coaxial SMA cables. A round cut-out in the PCB enables a 40 mm fan to be installed to provide sufficient cooling for the Red-Pitaya. Ventilation slots inside the aluminium enclosure ensure proper airflow.

The trigger input circuitry, described in section 4.3.4, was not included in the initial hardware design and was added at a later stage using hand-wiring and is therefore not visible in the Figures 4.4 to 4.5b

4.5 FPGA implementation

The FPGA represents the heart of the digital feedback system, in that it provides all the crucial signal processing needed for the application of active feedback. An outline

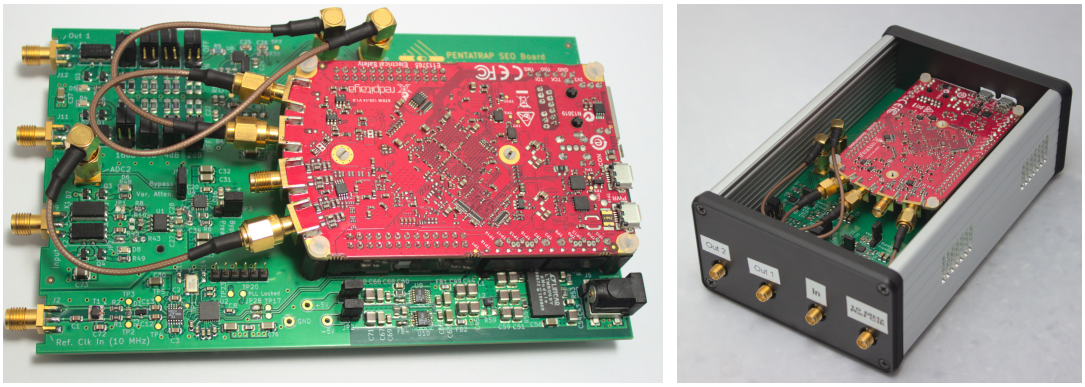

(a) (b)

Figure 4.5: Pictures of the feedback system with the Red-Pitaya (a) and assembled into the enclosure (b).

of the developed FPGA architecture is shown in Fig. 4.6. Most of the modules within the FPGA are connected to the CPU using the AXI Lite bus protocol (blue in Fig. 4.6), allowing them to be dynamically configured during run time.

The samples from the ADC are sent to the FPGA using a parallel 28 bit connection (two ADC channels with 14 bit each). An ADC interfacing module within the FPGA receives the sample data and converts them into the AXI stream protocol [56] (orange in Fig. 4.6), which is used for the entire real-time data transmission paths within the FPGA design. The datastream is subsequently split into two paths: One path leads into the *acquisition sytsem*, which provides a full-featured data acquisition system, providing downmixing and downsampling of the ADC samples and transfers them into a buffer region within the RAM of the Red-Pitaya, from where they can be further processed by the CPU. The second datapath is used as the actual real-time signal processing path between the ADC and the DAC for the realization of the active feedback. The block labeled *Feedback module* in Fig. 4.6 splits the ADC sample datastream into two separate outputs, which can be individually phase shifted and scaled in amplitude. The two output datastreams are then directly sent to the DAC using a DAC interfacing module. The acquisition system and the feedback module are further described in section 4.5.2 and section 4.5.1, respectively.

The feedback path can be configured to use an internal signal generator as the data source, allowing the generation of arbitrary sinusoidal test signals on the outputs of the feedback system. The signal generator is implemented using the direct digital synthesis (DDS) method [57]. An additional *trigger gate* within the feedback path allows to dynamically enable or diasble the active feedback using a dedicated FPGA input signal.

The development and synthesis of the FPGA design was carried out using the Xilinx Vivado toolkit. Almost the entire design was realized using the IP cores provided by Xilinx, resulting in a very fast development time of only a few days. The HDL code for interfacing with the ADC and DAC devices was taken from the “Red-Pitaya Notes” - an

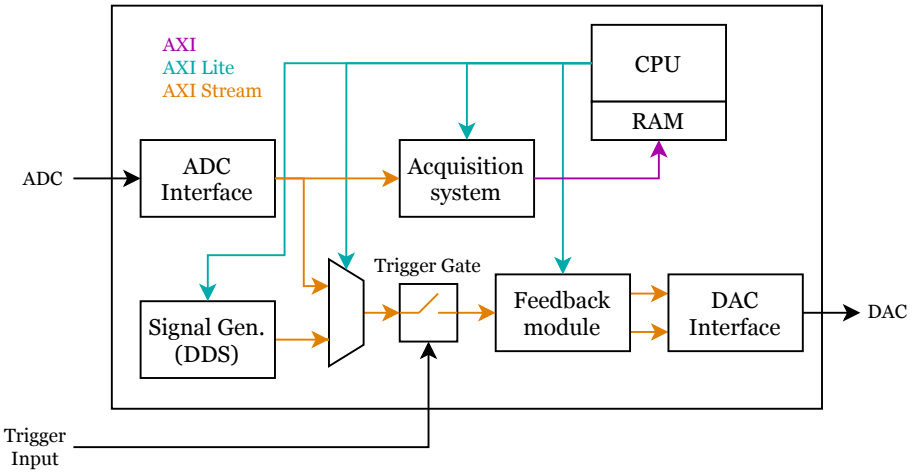

Figure 4.6: Block diagram of the FPGA implementation. For details see text.

extensive collection of FPGA IP cores, software and projects for the Red-Pitaya [58]. The only custom VHDL code that had to be written was for the dynamically configurable delay line, further discussed in section 4.5.1, and the trigger gate.
The utilization of FPGA resources used for the feedback system is shown in Tab. 4.2. As it can be seen, the utilization is not particularly high, which therefore opens the possibility to further extend the functionality of the feedback system in the future.

Table 4.2: Utilization of FPGA resources for the feedback system design on a Xilinx Zynq 7010 device.

	Utilization	
Resource	Absolute	Relative
LUT	4111	23.4 %
LUTRAM	739	12.3 %
FF	6472	18.4 %
BRAM	20.5	34.2 %
DSP	50	62.5 %
IO	54	54.0 %
PLL	1	50.0 %

4.5.1 Feedback module

The feedback module of the FPGA implementation features two individual datapaths, each providing the possibility to introduce a variable phase shift and to scale the signal amplitude.

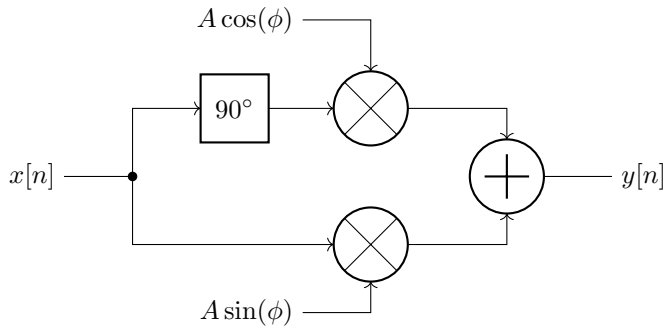

Figure 4.7: Block diagram representation of the phase shifter. The 90° phase shifter is implemented using a delay line, as described in the text.

The variable phase shifter is realized by first generating a constantly 90° phase-shifted copy of the input signal and then summing the original and the shifted signal, subsequently refered to as the *inphase* and *quadrature* components, with adjustable weights, as depicted in Fig. 4.7. By weighting the inphase component with $\sin(\phi)$ and the quadrature component with $\cos(\phi)$, the summed output signal will be phase shifted by ϕ with respect to the input signal. Applying a common scaling factor A to both signal paths leads to a scaling of the output signal.
The difficulty of this concept lies in the implementation of the 90° phase shifter. An ideal 90° phase shift over all frequencies can be mathematically described as the Hilbert transform [59] $H\{x\}$ of the input signal x. In the frequency domain it can be represented as a simple multiplication with the imaginary constant j:

$$H\{X(\omega)\} := -j\,\mathrm{sgn}(\omega)\,X(\omega)\,. \tag{4.3}$$

However, its time domain representation $h\{x(t)\} = x(t) * \frac{1}{\pi t}$ reveals that the Hilbert transform is a non-causal transform, making it impossible to implement it on the FPGA. Fortunately, as the feedback system only needs to operate at a very narrow bandwidth (see section 4.1), the 90° phase shift can be validly approximated using a simple time delay

$$y[n] = x[n - D]\,, \tag{4.4}$$

with D being the number of samples that should be delayed. For a system with a data rate of ν_{rate}, the number of required delay taps D can be calculated using

$$D = \left\lfloor \frac{90}{360} \frac{\nu_{\mathrm{rate}}}{\nu_{\mathrm{signal}}} \right\rceil\,, \tag{4.5}$$

resulting in the best approximation of a 90° phase shift in the proximity of the expected signal frequency ν_{signal}.
By combining the time domain representation Eq. (4.4) of the previously described 90° phase shifter with the model of the variable phase shifter stage shown in Fig. 4.7, the

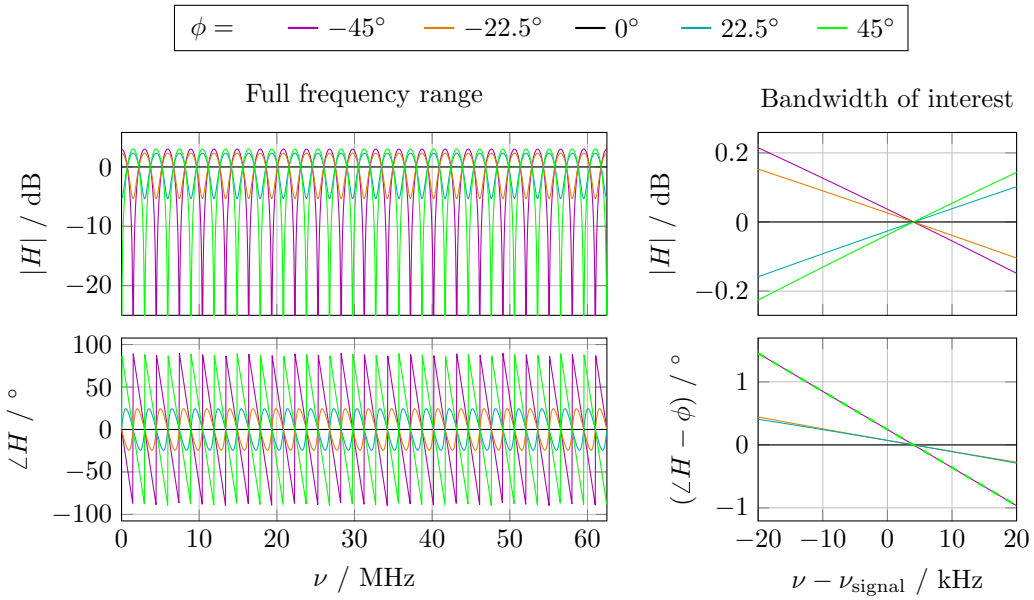

Figure 4.8: Amplitude and phase response of the variable phase shifter for different phase shifts ϕ. The data rate is $\nu_{\text{rate}} = 125\,\text{MHz}$ and the signal frequency was chosen to be $\nu_{\text{signal}} = 740\,\text{kHz}$, resulting in an optimal fixed delay of $D = 42$. The left graphs represent the full frequency range, while the right graphs is zoomed to the frequency range in the proximity of ν_{signal}. The zero crossing points seen in the right graphs is shifted from ν_{signal} due to rounding in Eq. (4.5).

difference equation

$$y[n] = A(\cos\phi\, x[n] + \sin\phi\, x[n-D]) \tag{4.6}$$

can be found. Applying the Z-transform results in the complex frequency-domain transfer function

$$H(z) = \frac{Y(z)}{X(z)} = A\left(\cos\phi + \sin\phi\, z^{-D}\right), \tag{4.7}$$

with a region of convergence (ROC) of $\{z \neq 0\}$. By evaluating $H(z)$ on the unit circle $|z| = 1$, the frequency response can be determined. For that, we substitute $z = e^{j\omega}$, resulting in

$$H(e^{j\omega}) = A\left(\cos\phi + \sin\phi\, e^{-j\omega D}\right). \tag{4.8}$$

The amplitude response can be easily derived by evaluating the absolute value of $H(e^{j\omega})$:

$$|H(e^{j\omega})| = A\sqrt{1 - \sin(2\phi)\,\cos(\omega D)}\,. \tag{4.9}$$

It can be seen, that the amplitude response is not perfectly flat, but is superimposed with exactly $D/2$ amplitude minima over the frequency range $0 \leq \omega \leq \omega_{rate} = 2\pi\nu_{\text{rate}}$. However, in the close proximity of $\omega_{\text{signal}} = 2\pi\nu_{\text{signal}}$, the $\cos(\omega D)$ term becomes very

small, making the amplitude response approximately flat in this region (see Fig. 4.8). Furthermore, due to the constant group delay introduced by the fixed 90° phase shifter, the phase response is not flat either. However, as it can be seen from Fig. 4.8, the phase deviation in the proximity of ν_{signal} is comparably small.

4.5.2 Acquisition system

A full-featured acquisition system was integrated into the FPGA implementation, providing the possibility to record the ADC samples into a memory buffer which can be accessed from the CPU. This enables, among other things, the implementation of data analysis and control algorithms within the same device that provides the active feedback functionality. In section 4.6.1, a control loop for a single-ion self excited oscillator is described, which would not have been possible without this acquisition system.
As the expected signal from the axial oscillation has a very low fractional bandwidth of FBW $= BW_{\text{ion}}/\nu_z < 1.4 \cdot 10^{-5}$ (assuming $\nu_z \approx 740\,\text{kHz}$, $\text{BW}_{\text{ion}} < 10\,\text{Hz}$), a digital downmixer was implemented within the acquisition system to provide an efficient way to sample this narrow bandwidth signal. For that, the datastream of ADC samples is initially downmixed using an IQ-mixer architecture (inphase/quadrature mixer), as can be seen in Fig. 4.9. Compared to a single-mixer architecture, this provides the benefit of improved image frequency rejection and enables to mix the signal of interest down to 0 Hz while keeping its left-sided spectrum. A direct digital synthesizer (DDS), generating a sine and a cosine output, is used as the local oscillator for the mixer. The inphase and quadrature baseband signals that come out of the mixing stage are subsequently downsampled using a pair of cascaded integrator-comb (CIC) filters [60] to reduce the datarate. These filters were designed to be be freely configurable for downsampling ratios within the range of 4 to 4096. As the frequency response of CIC filters is not perfectly flat, a pair of finite impulse response (FIR) compensation filters were added to flatten out the frequency characteristics. The 309 coefficients for the FIR filters were taken from [58]. The FIR filters provide an additional rate reduction of factor two.
The downmixed and downsampled datastream is then directed through a FIFO buffer (first-in first-out) into the DMA (direct memory access) engine, which writes the datas-

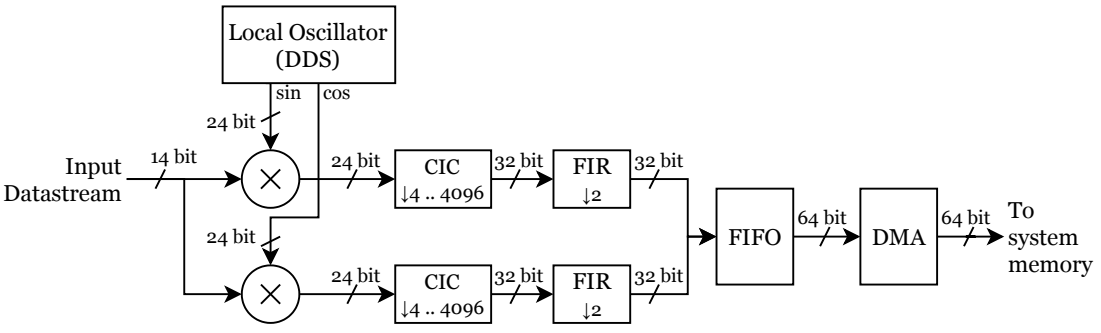

Figure 4.9: Block diagram of the acquisition system.

tream into a predefined address range within the system memory of the Red-Pitaya. The FIFO buffer prevents data loss in cases when the DMA engine is not directly able to write the data into the system memory e.g. due to an occupied memory bus or low write priority of the DMA.

4.6 Software implementation

A python library was written to provide access to the individual modules within the FPGA. It enables the dynamic configuration of the feedback path, the signal generator and the acquisition system. Furthermore it provides the data structures and methods needed to access the data stored inside the system memory by the acquisition system. As described in section 4.5, the individual modules within the FPGA are connected to the CPU using an AXI lite bus, which is directly accessible from the Linux operating system using physical address mapping. The python library basically provides an abstraction layer to this raw physical address access.
The library can be directly used through a Jupyter-Notebook server running on the Red-Pitaya, providing an interactive and flexible possibility for programming measurement tasks. An additional layer on top of the python library provides remote access to the feedback system using the EPICS (Experimental Physics and Industrial Control System) network protocol [61]. This allows the feedback system to be easily integrated into the PENTATRAP control system, which is already based on the EPICS protocol [62, 41].

4.6.1 Single-ion self-excited oscillator control loop

In the context of Penning-trap experiments, a self excited oscillator (SEO) describes the process of applying positive feedback directly to the ion in order to cancel out the damping forces acting on it. A theoretical description of the characteristics of an ion under active feedback was presented in section 2.5.2. There it is shown, that the damping of the ion can be cancelled completely if a feedback gain of

$$G = \frac{D_{\mathrm{eff,fb}}}{D_{\mathrm{eff}}} \tag{4.10}$$

is applied. $D_{\mathrm{eff,fb}}$ and D_{eff} denote the effective electrode distance, introduced in section 2.4.1, of the feedback and detection electrode, respectively. In practice, every minor deviation from this value will result in an exponential increase or decrease of the motional amplitude of the ion. To counteract this, the feedback gain has to be constantly adjusted. Therefore, a PID control loop was implemented in software, which constantly monitors the amplitude of the ion, compares it with an amplitude set point and adjusts the feedback amplitude accordingly. The amplitude of the ion is obtained using the internal acquisition system of the FPGA: The downmixing and downsampling of the acquisition system is configured to achieve the highest possible frequency resolution of the ion signal (Local oscillator frequency set to ν_z; Downsampling rate set to 4096). After collecting 4096 samples and transforming them into the frequency domain using

a fast-fourier-transform (FFT), the rough position of the ion peak signal is found by searching for the maximum value within the amplitude spectrum. Combining this value with the values of its two neighboring frequency bins, the peak amplitude is estimated using a quadratic interpolation [63]. As a side effect, the quadratic interpolation also provides an estimate of the axial frequency of the ion.
The first test of the SEO procedure is presented in section 6.2. A control loop rate of 12.5 Hz could be achieved. The self excited oscillator technique makes it possible to determine the axial frequency at a very high rate, e.g. for the detection of spin-flips [64] or to monitor fluctuations of the trap potential U_0.

4.7 Integration into the PENTATRAP experiment

The input signal for the feedback system is directly derived from the amplified axial ion signal using the auxiliary output port of the axial detection electronics, described in section 3.4. Although the feedback is intended to be solely applied to trap 2, the lower end cap (LEC) electrode of trap 1 had to be used for one of the feedback channels. This is due to noise problems within the detection circuit when using the upper end cap (UEC) electrode as a feedback or excitation electrode. The second feedback channel is connected to the lower correction electrode (LCE) of trap 2. An additional −10 dB attenuator is used within the second feedback path to accommodate for the smaller distance, and thus higher coupling factor, of the LCE of trap 2 to the ion's center of motion position.
The reference clock of the feedback system is generated by a FS725 rubidium frequency standard. The trigger pulses, required for certain measurements techniques (e.g. the APnP technique introduced in chapter 5), are generated using a *Stanford Research DG645* digital pulse generator.

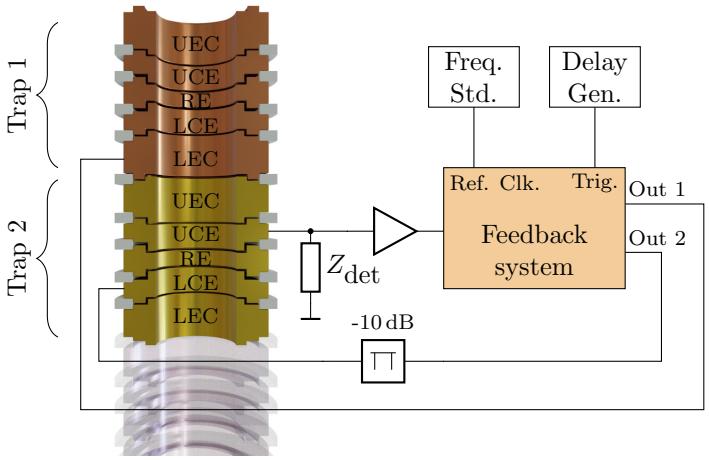

Figure 4.10: Connection diagram of the feedback system integrated into the PENTATRAP experiment

5

Phase-Sensitive Axial Frequency Determination

A phase-sensitive technique for the determination of the modified cyclotron frequency, called *PnP*, was introduced in section 2.4.4. Due to the high precision of this technique, the uncertainty of the modified cyclotron frequency no longer poses the limiting factor for the Pentatrap experiment. As can be seen in Eq. (2.12), the second highest weighted contribution to the total uncertainty of the free cyclotron frequency is the uncertainty of the axial frequency. In fact, it turns out that the accuracy of Pentatrap is currently mainly limited by the uncertainty of the axial frequency determination.
In this chapter, a phase-sensitive detection technique for the axial mode is introduced, which inherently has the potential to outperform the currently used single-dip measurement technique (described in section 2.4.3) in terms of measurement speed and precision. Due to its similarities with the PnP method, this technique will be shortly called *APnP* (Axial Pulse and Phase) within the context of this thesis.

5.1 Adaptation of the PnP technique for axial measurements

The basic three-step process of the PnP technique can be almost equally applied for the detection of the axial frequency: After an initial dipolar excitation with a well-defined phase (phase imprint), the ion's axial oscillation is allowed to evolve (phase evolution) for the duration t_{evol} after which its phase is read out using the axial detection system (phase readout). However, as the axial mode is permanently coupled to the detection system, the ions axial motional energy will exponentially decay during the phase evolution time, due to resistive cooling. The rate of this decay, characterized by the cooling time constant τ (Eq. (2.22)), limits the achievable phase evolution time to impractically small values, typically in the order of a few 100 ms. This limitation can be overcome by decoupling the ion from the detection system for the duration of the phase evolution time and thus preventing it from cooling in. This concept has been originally proposed in [65] but could not be implemented due to the lack of technical possibilities to decouple the ion from the detection electronics.
The feedback system introduced in chapter 4 provides multiple ways to achieve this:

1. **Resonator frequency shift:** The application of active feedback to the resonator allows to deliberately shift its resonance frequency away from the ions axial frequency. This way, the damping of the ion becomes minuscule, effectively leading to a decoupling of the ion from the detection electronics.
2. **Resonator Q variation:** The Q-factor of the resonator can be reduced using active feedback, leading to a decrease of the ion's damping. However, as the minimal achievable Q-factor is limited (see section 2.5.1), this method can not be used to allow arbitrarily long phase evolution times.
3. **Ion self excitation:** By coupling positive feedback directly to the ion, as described in section 2.5.2, the damping of the ion can be minimized or completely cancelled.

While all the listed techniques can potentially be utilized to implement the APnP technique and should therefore be individually evaluated and compared to each other, only the resonator-shift technique (1) was tested within the work of this thesis.
At the beginning of an APnP measurement cycle, shown in Fig. 5.1, the center frequency ν_{res} of the resonator is shifted away from ν_z by multiple resonator linewidths. This allows the ion to freely oscillate during the phase evolution time, after it has been excited using a phase imprint pulse. It must be noted, that the axial frequency of the ion is slightly modified due to the frequency pulling effect (see section 2.4.2) induced by the resonator detuning. However, this effect is well understood and can therefore be corrected for during data analysis [28]. After the phase evolution time, the resonator is switched back to the axial frequency, in order to be able to detect the ion. A fast switching time is required to minimize the duration the ion is experiencing dynamic frequency pulling effects.

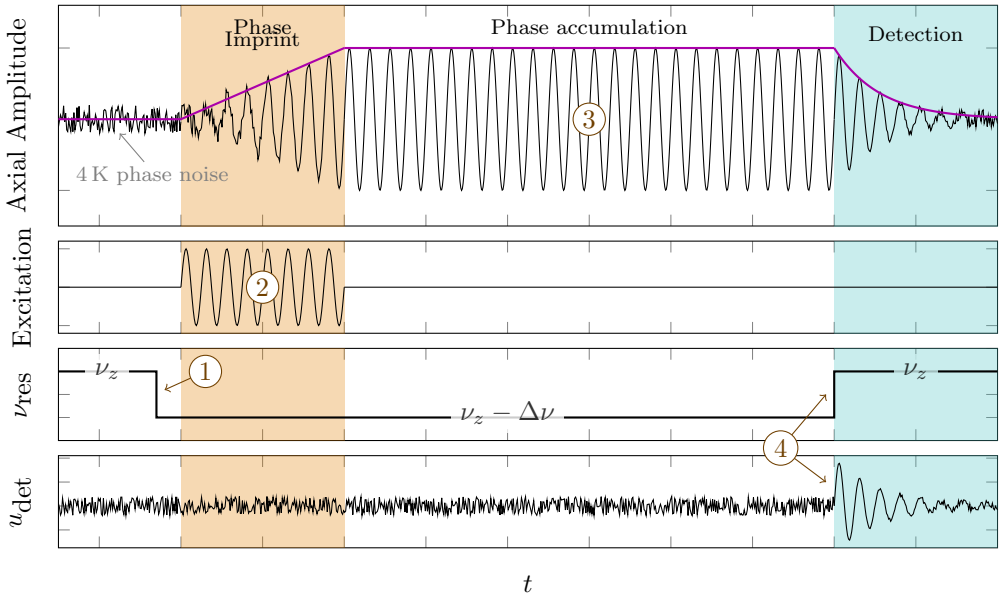

Figure 5.1: Conceptual timing diagram of an APnP measurement cycle: 1. shift resonator center frequency by $\Delta\nu$; 2. phase imprint using dipolar excitation pulse; 3. phase accumulation; 4. shift resonator back to ν_z and read out phase. u_{det} denotes the voltage at the detection circuit.

The statistical frequency uncertainty achievable using the APnP technique is given by

$$\sigma\{\nu_z\} = \frac{\sigma\{\Delta\phi\}}{2\pi\, t_{\mathrm{evol}}}\,, \tag{5.1}$$

with $\sigma\{\Delta\phi\}$ being the uncertainty of the phase difference determination. Obviously a larger phase evolution time t_{evol} is favorable in order to achieve higher frequency precision. However, the phase evolution time can not be increased arbitrarily, as any random frequency fluctuations, originating from instabilities of the trapping potential U_0, accumulate over time and lead to an increasing phase uncertainty $\sigma\{\Delta\phi\}$.
As Eq. (5.1) reveals, the APnP method can be used to determine the axial frequency to a greater precision than the Fourier limit would allow, assuming $\Delta\phi$ can be determined to less than 2π uncertainty [65]. The achievable precision is only limited by the Cramér–Rao information bound [66, 67].
One drawback of this technique is the large axial amplitude of the ion resulting from the phase imprint pulse. Although an ideal harmonic oscillator is completely amplitude independent, unavoidable effects like trap potential anharmonicities and relativistic shifts introduce an amplitude dependency and therefore lead to systematic shifts of the axial frequency [33]. Additional statistical uncertainties arise from the random starting conditions of the ions motional state and the finite repeatability of the excitation pulse.

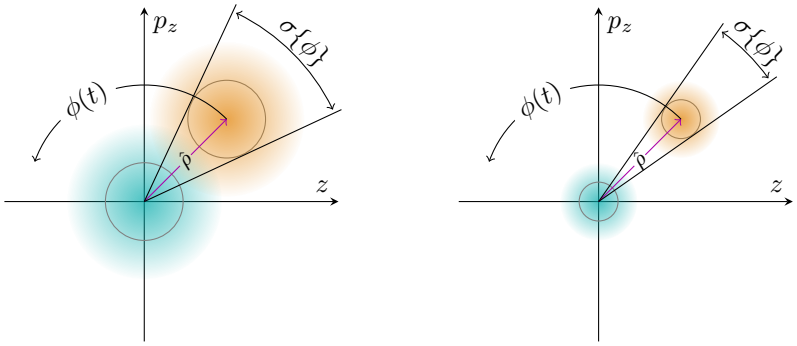

(a) **(b)**

Figure 5.2: Representation of the ions motional states within its phase space (axial position z and axial impulse p_z). The blue and orange dots represent the probability densities of the cooled and excited motional state at t_0, respectively. Figure (a) qualitatively represents an ion cooled to 4 K, while figure (b) represents an initially actively cooled ion. In both figures the ions are assumed to be excited to the same amplitude $\hat{\rho}$.

5.2 Reducing phase uncertainty with active feedback cooling

The systematic shifts and statistical uncertainties described in section 5.1, can be minimized by actively cooling the axial mode below 4 K prior to the APnP cycle. This shrinks the probability distribution of the ion's initial motional state, as illustrated in Fig. 5.2. Therefore, after applying the phase imprint pulse, the phase can be determined with smaller uncertainty $\sigma\{\phi\}$. Alternatively, this opens up the possibility to use smaller excitation amplitudes, resulting in lower systematic shifts, while still maintaining low phase uncertainties.
This extension of the APnP technique requires the feedback system to support three individual feedback configurations (cooling, resonator shift, no feedback), which must be dynamically and precisely interchanged during the APnP cycle. Unfortunately, due to time constraints, this feature could not yet be implemented into the feedback system.

6

Measurements and Results

In this chapter, various measurements for the characterization of the active feedback system in connection with the Pentatrap experiment are presented.
Section 6.1 covers the effects of active feedback applied to the resonator of the axial detection system for different feedback parameters. In particular, the results of resonator frequency shifting and active feedback cooling are presented and analyzed. Section 6.2 describes the setup procedure and the operation of a single-ion self-excited oscillator and analyzes the achieved amplitude and frequency stability. Finally, the results of the first APnP measurement cycles are presented in section 6.3.
All measurements were carried out using the setup shown in section 4.7. The measurements that involved ions were carried out with rhenium-187 in a highly charged state of 30+, produced in the DreEBIT (see section 3.1). However, the particular choice of ion species and charge state is arbitrary and not of special interest for the results.

6.1 Resonator feedback

6.1.1 Parameter space characterization

Initially, the response of the resonator to a broad range of feedback parameters was measured. For that, a 128×128 grid composed of feedback gain/phase pairs, hereinafter referred to as the *parameter space*, was scanned while evaluating the corresponding characteristics of the resonator.
For each point within the parameter space, a set of 40 FFT spectra with 4096 frequency bins over a frequency range of ≈15 kHz were acquired using the feedback system's own acquisition capabilities. After they were averaged into a set of 128×128 low variance spectra, the resonator parameters were obtained for each datapoint by fitting an appropriate physical model to the spectra. For that, a model described in [68] was used:

$$a(\nu) = 10 \log_{10} \left[A_{\mathrm{res}} \left(1 + Q^2 \left(\frac{\nu^2}{\nu_{\mathrm{res}}^2} - 2 + \frac{\nu_{\mathrm{res}}^2}{\nu^2} \right) \right)^{-1} + A_{\mathrm{noise}} \right] . \tag{6.1}$$

The model includes parameters for the resonator's Q-factor, resonance frequency ν_{res}, its amplitude at resonance A_{res}, as well as the noise floor amplitude A_{noise} of the spectrum. The obtained results are presented in Fig. 6.1 as a heat map of the parameter space. When analyzing the results qualitatively, a close correlation to the theoretical calculations, shown in Fig. 2.7, can be seen. However, the experimental results reveal an additional phase shift of ≈100°, which can be attributed to unknown phase shifts within the axial detection system of Pentatrap. As the absolute gain factor of the complete feedback path has not been calibrated, the *Gain* parameter shown in Fig. 6.1 must be interpreted as a relative quantity. The black regions in Fig. 6.1 represent the areas of free oscillation of the resonator. This was detected by analyzing the noise floor of the spectrum: The large amplitude of the resonator in free oscillation leads to signal clipping within the amplifiers and the ADC of the acquisition system, resulting in a distortion of the acquired signal. This can be seen as an apparent decrease of the noise floor amplitude within the spectrum. Therefore, all datapoints with a noise level below a certain threshold were considered to represent resonator oscillation. The results of this characterization measurement opened up the possibility for further, more specialized tests of the resonator feedback, described in the next sections.

6.1.2 Frequency shift

Setting the phase shift of the feedback system to $\approx -100°$ results in a real feedback phase of $\approx 0°$ due to the additional phase shift described in section 6.1.1. This feedback configuration allows to arbitrarily modify the resonance frequency of the resonator by varying the feedback gain. For the measurement described in this section, the gain was adjusted to produce a frequency shift of ≈ 2.8 kHz.

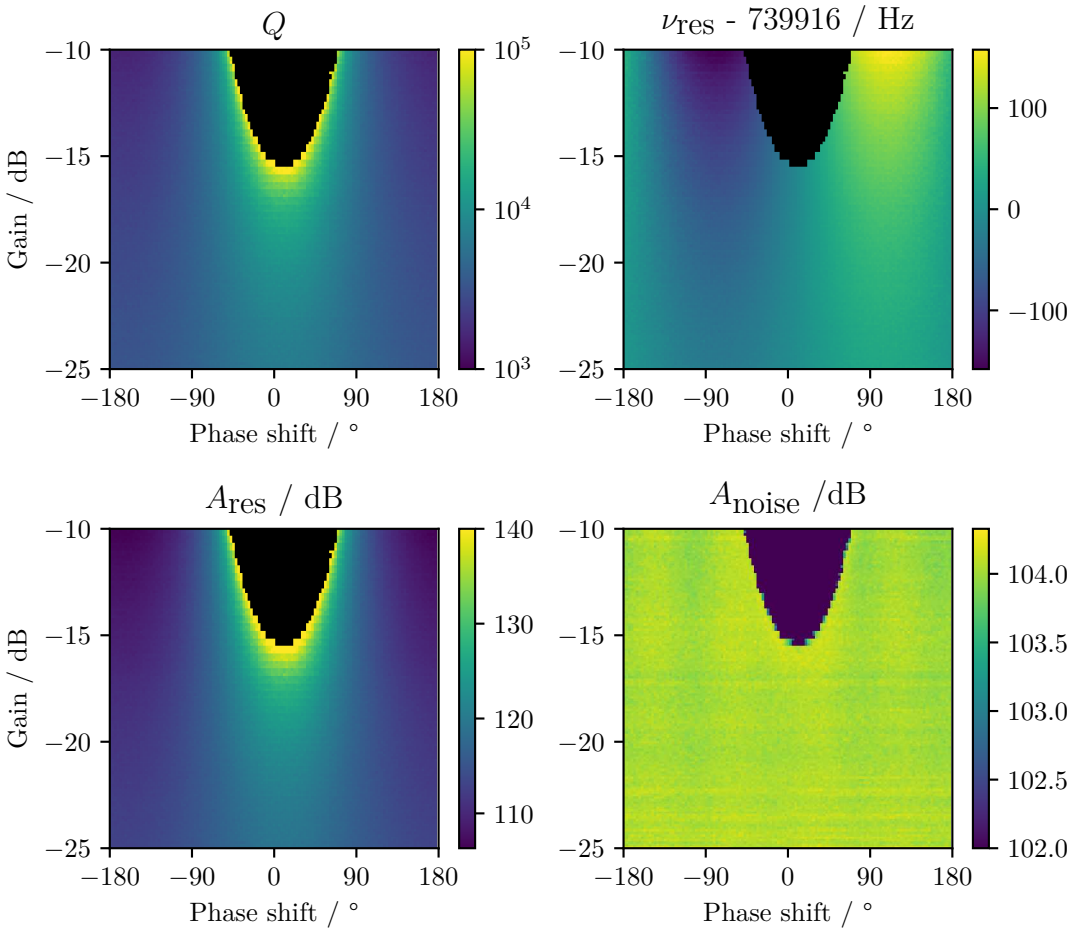

Figure 6.1: Measured resonator characteristics, namely the Q-factor, resonator center frequency ν_z, resonance amplitude A_{res}, and background noise amplitude A_{noise}, for a wide range of different feedback parameters. The black regions indicate the parameters for which the resonator has been driven into free oscillation.

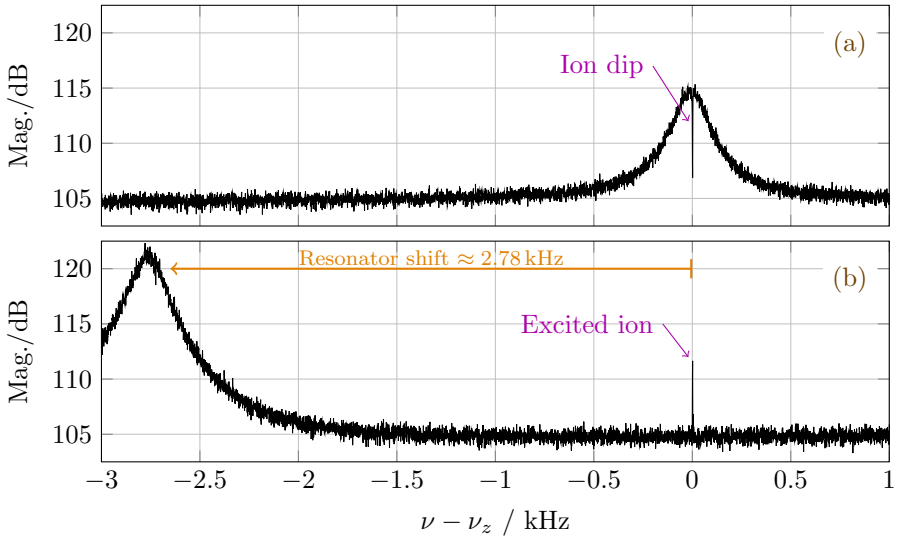

Figure 6.2: Noise spectrum of the resonator without (a) and with enabled active feedback (b).

Figure 6.2 presents the result of the frequency shift by comparing it with a resonator spectrum without active feedback enabled. In both cases, a $^{187}Re^{30+}$ ion is visible at ν_z: In Figure 6.2a it appears as a dip in the noise spectrum while the ion in Figure 6.2b had to be first excited to a rather large amplitude in order to be visible as a peak. In the latter case, the ion peak was visible for several minutes, indicating a significant reduction of the damping due to the shifted resonator. Besides being shifted in frequency, the amplitude of the resonator with enabled feedback was increased by $\approx 6\,\mathrm{dB}$ compared to the normal resonator. This can be attributed to a non-perfectly adjusted feedback phase and to the additional noise contributions of the active feedback.

6.1.3 Q-factor variation

By applying active feedback with a theoretical phase shift of $-90°$ ($\approx 10°$ in Fig. 6.1), the Q-factor of the resonator can be manipulated. Figure 6.3 shows the obtained results for $-90°$ feedback with different feedback gains. The listed gain factors $\tilde{G}$ are only intended as a relative measure for comparison of the results. They do not represent the absolute feedback gain. Each measurement consists of 22 FFT spectra that were averaged and subsequently fitted with the model presented in Eq. (6.1), resulting in the Q-factors listed in Tab. 6.1. Combining the resulting Q-factors with the relations presented in Eq. (2.16) and (2.39) with the parameters listed in Tab. 3.2, an effective resistance R_{eff} and temperature T_{eff} of the resonator was assigned to each measurement in Tab. 6.1. The quoted uncertainties originate from the parameter variance of the resonator fit. As the resonator is cooled with liquid helium, the temperature without active feedback ($\tilde{G} = 0$) has been assumed to be exactly $4.2(0)\,\mathrm{K}$. Although its actual

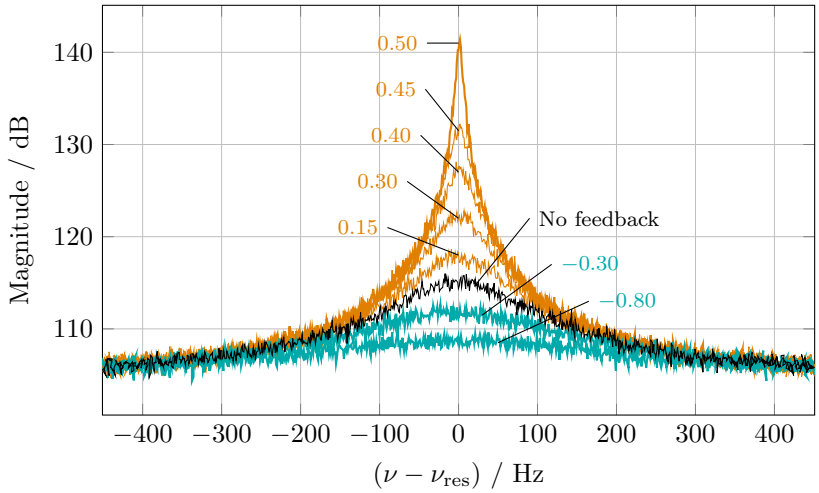

Figure 6.3: Noise spectrum of the resonator with −90° active feedback for different relative feedback gains $\tilde{G}$. The orange and blue colored spectra represent positive and negative feedback gains, respectively.

physical temperature might be slightly higher, the results shown in Tab. 6.1 still provide a good estimate of the achievable temperatures when using active feedback. The lowest achieved temperature of 1.72(4) K might potentially be further reduced with higher feedback gain settings.

Table 6.1: Results of the resonator Q-factor variation measurement using active feedback with relative gain $\tilde{G}$. For each measurement, an effective resonator resistance R_{eff} and temperature T_{eff} has been calculated, as described in the text.

$\tilde{G}$	$Q/10^3$	R_{eff}/ MΩ	T_{eff}/ K
0.50	93.6(23)	609(15)	88.1(21)
0.45	31.92(49)	207.9(32)	30.06(46)
0.40	18.79(24)	122.4(16)	17.70(23)
0.30	10.54(11)	68.65(73)	9.93(11)
0.15	6.31(7)	41.05(44)	5.94(6)
0.00	4.46(5)	29.04(28)	4.20(0)
-0.30	2.83(4)	18.41(24)	2.66(3)
-0.80	1.83(4)	11.89(16)	1.72(4)

6.2 Single-ion self-excited oscillator

This section describes the setup procedure and the operation of a single-ion self-excited oscillator (SEO), which can be used to constantly keep the axial motion of an ion excited to a predefined amplitude for an arbitrarily long time. This is accomplished by coupling active feedback directly to the ion (see section 2.5.2) so that its damping constant γ becomes zero, and therefore its cooling time constant τ tends towards infinity. In order for this to work, the direct coupling of the feedback signals to the resonator first has to be cancelled out in a process called *resonator feedthrough cancellation*, as it has been introduced in section 2.5.3.
For that, the internal signal generator of the feedback system was set up to produce a sine wave at a frequency close to ν_z on both outputs. The generated signal was clearly visible as a large peak within the spectrum acquired using the acquisition module of the feedback system. By carefully adjusting the phases ($\phi_{\mathrm{fb},1}$, $\phi_{\mathrm{fb},2}$) and gains ($G_{\mathrm{fb},1}$, $G_{\mathrm{fb},2}$) of the feedback outputs with respect to each other, the amplitude of the signal appearing in the spectrum was iteratively decreased until it disappeared completely. At that point, the feedback system was switched back to normal feedback operation mode (disabled internal signal generator), which no longer had an effect on the resonator parameters due to the resonator feedthrough cancellation. For the setup described in section 4.7, the optimal parameters were found to be

$$\phi_{\mathrm{fb},1} - \phi_{\mathrm{fb},2} = 194^\circ\,, \tag{6.2a}$$

$$\frac{G_{\mathrm{fb},1}}{G_{\mathrm{fb},2}} = 0.881\,. \tag{6.2b}$$

As long as these relations are met, the feedback parameters can be freely varied without compromising the feedthrough cancellation performance.
After the successful optimization of the resonator feedthrough cancellation, a $^{187}\mathrm{Re}^{30+}$ ion was loaded into the Penning trap. In order for the SEO to properly work, the feedback phase, as experienced by the ion, has to be adjusted to exactly 180°. Equation (2.46) shows that the axial frequency of the ion will be detuned for all feedback phase settings except for the 0° or 180° case. Therefore, by monitoring the ion dip spectrum while iteratively adjusting the feedback phase (adhering to the relation shown in Eq. (6.2a)) until the frequency detuning goes to zero, the feedback settings for either 0° or 180° were found. Using the fact that 180° feedback leads to a reduction of the ion damping (see Eq. (2.45a)) and therefore to a decrease of the ion dip width, the correct settings for 180° feedback were found.
After the initial setup of the feedback parameters, the SEO procedure, previously introduced in section 4.6.1, was tested. The amplitude set point A_{set} was chosen to be 3 dB higher than the amplitude of the resonator lineshape. This turned out to be a good compromise in order for the control loop to clearly distinguish the ion peak from the resonator noise while still being low enough to not cause major frequency errors due to trap anharmonicities.

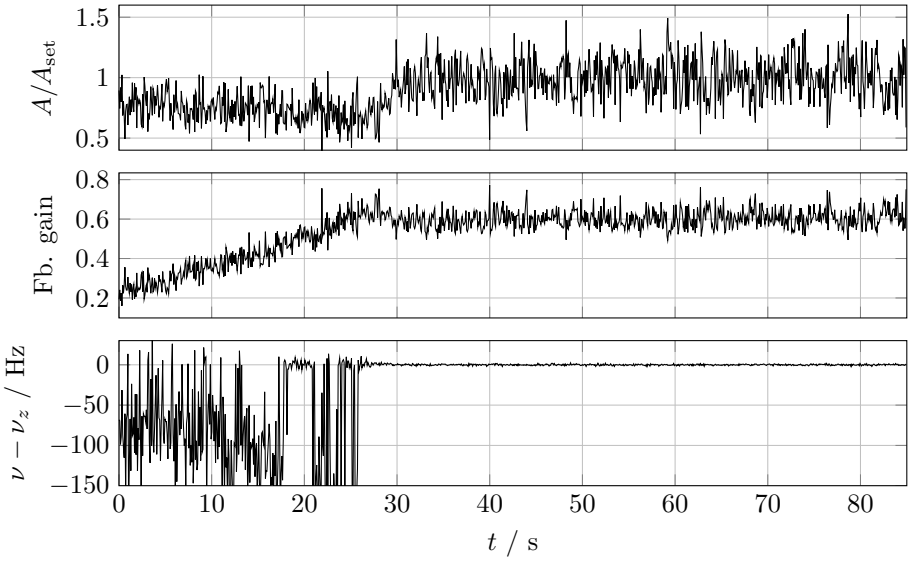

Figure 6.4: Time evolution data of the ion under self-excitation. The upper graph shows the ratio of the measured amplitude A to the amplitude setpoint A_{set}, the graph in the middle shows the relative feedback gain, and the lower graph shows the difference of the measured peak frequency ν to the theoretical axial ion frequency ν_z.

Figure 6.4 shows the ion axial amplitude A, the relative feedback gain $\tilde{G}$ and the measured axial ion frequency ν during the operation of the self-excited oscillator. At $t = 0$ the SEO control loop starts to slowly ramp up the feedback gain until a distinct ion peak becomes visible above the background noise of the resonator at $t \approx 29\,\mathrm{s}$. After that, the control loop constantly adjusts the feedback gain in order to regulate the amplitude of the ion to the set point A_{set}. The equilibrium condition, at which the ion damping is exactly cancelled out, was found at $\tilde{G} \approx 0.6$. However, due to the cancelled ion damping, any noise contributions from the thermal noise of the resontor or from the feedback system itself will directly lead to amplitude fluctuations of the ion. These residual amplitude fluctuations have a standard deviation of $\sigma\{\frac{A}{A_{\mathrm{set}}}\} = 0.17$ within the interval $30\,\mathrm{s} \leq t \leq 85\,\mathrm{s}$. At the same time, the standard deviation of the frequency fluctuations have been found to be $\sigma\{\nu\} = 0.75\,\mathrm{Hz}$. Figure 6.5 shows a statistical representation of both the amplitude and frequency measurements. It can be seen that there is no correlation between the amplitude and the frequency fluctuations, as it would be the case if the frequency fluctuations were indirectly caused by the amplitude fluctuations due to trap anharmonicities. Instead, the frequency fluctuations might be caused by a non-perfectly stable sampling frequency, as the feedback system was not connected to the external 10 MHz frequency standard at the time of the SEO measurements.

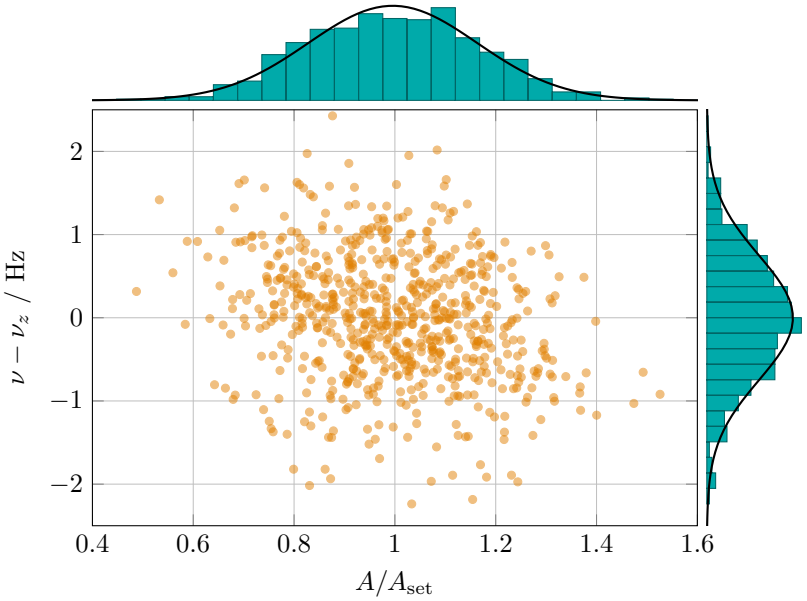

Figure 6.5: Distribution of the amplitude and frequency fluctuations of the ion peak during self excitation. The black lines on top of the histograms represent the Gaussian distribution fitted to the data.

6.3 First test of the APnP measurement technique

This section describes the first test of the APnP measurement technique, theoretically described in chapter 5, that was carried out using the digital feedback system.

Test setup

The phase readout of the APnP cycle was realized using the FFT analyzer of the PENTATRAP experiment. A digital pulse generator (DG645) provides precisely timed trigger pulses for the control of the feedback system, the excitation pulse generator and the FFT analyzer. Except for the feedback system, the measurement setup of the APnP technique is similarly used for the standard PnP measurements (see section 2.4.4) and is therefore extensively tested and is not expected to introduce major unknown systematic errors.

The feedback system was configured to shift the resonator by $\approx 2\,\text{kHz}$ when it is triggered by the pulse generator. The phase imprint pulse is generated by a function generator (Keysight 33500B) configured to output a 500 µs sine wave burst at a frequency of $\nu_z = 740.2\,\text{kHz}$ and an amplitude of 1 V.

Procedure

To generally proof the feasibility of the APnP measurement scheme, two measurements with phase evolution times of 11 ms and 21 ms have been carried out. The comparably

short phase evolution times were chosen in order to test if the dynamic switching of the resonantor feedback during the phase readout has any effect on the phase stability of the ion. For each measurement, a total of 20 phase values have been acquired using 20 subsequent APnP cycles. After each cycle, a 1 s dwell time with disabled active feedback was provided in order to allow the ion to cool back down to 4.2 K.

Result

The results of the APnP measurements are listed in Tab. 6.2. In order to determine the axial ion frequency from these results, the phase values must be first unwrapped, as previously mentioned in section 2.4.4. However, as this process requires more measurements with a wider variety of phase evolution times, the axial frequency could not be obtained from the presented results. Therefore, the absolute values of the averaged phases $\langle\phi\rangle$ are not of special interest for the following discussion. Unfortunately, due to problems with the ion transport and the ion lifetime within the trap, no further measurements could be carried out within the time frame of this thesis.
However, analyzing the standard deviations of the measurement results provides some insight into the performance and possible deficits of the APnP technique: The deviations of both measurements is found to be well below 360°, revealing, that the phase information of the ion has not been significantly altered by the dynamic shift of the resonator. A phase uncertainty of 13° for the 11 ms evolution time measurement can be considered to be a very precise result and is similar to the phase uncertainties obtained in the standard cyclotron PnP technique. However, the large increase of the phase uncertainty in the $t_{\mathrm{evol}} = 21\,\mathrm{ms}$ measurement is an indication for fluctuations of the axial frequency during the phase evolution time. In fact, it was found that a recent design change within the voltage supply for the trap electrodes caused the trap potential U_0 to be unstable, and therefore lead to a fluctuating axial frequency. If the original stability of the voltage source ($\frac{\delta V}{V} \approx 2 \cdot 10^{-8}$ [69]) can be recovered, the APnP technique is expected to achieve significantly smaller phase uncertainty and will therefore lead to a great improvement of the axial frequency determination precision.

Table 6.2: Results of the first APnP phase measurements for two different evolution times t_{evol}. Each measurement consisted of 20 APnP cycles that have been combined, resulting in an average phase $\langle\phi\rangle$ with a standard deviation $\sigma\{\phi\}$.

t_{evol}	$\langle\phi\rangle$	$\sigma\{\phi\}$
11 ms	291.1°	13°
21 ms	305.1°	40°

7

Summary and Outlook

In the course of this thesis, an active feedback system for ion manipulation in a Penning trap was developed and successfully integrated into the PENTATRAP experiment. The application of feedback proved to be a versatile tool, allowing to modify the characteristics of the ion detection system and to directly influence the damping forces acting on the ion.

The feedback system was implemented using a new concept, making extensive use of real-time digital processing algorithms on an FPGA. One of the core components of the FPGA architecture is the variable phase shifter, which was mathematically examined for its frequency response. Within the evaluated bandwidth of 40 kHz around the expected axial frequency of the ion, the amplitude and phase response show a weak linear frequency dependency with a maximum deviation of ± 0.2 dB and $\approx \pm 1°$, respectively. Considering the very narrow bandwidth of the ion detection system of a few 100 Hz, this frequency dependency is negligible. The digital feedback system was designed to by synchronized to an external reference clock, leading to a high temporal stability of the feedback operation. Furthermore, the digital implementation opens up the possibility for highly dynamic variation of feedback parameters during runtime, which was hardly possible with previously used analog feedback systems. Additionally, a complete data acquisition system was integrated into the FPGA logic, which is used for the implementation of a single-ion self-excited oscillator. The SEO is based on the application of positive feedback coupled directly to the axial mode of the ion, leading to a significant reduction of its damping. At a specific feedback gain, the damping is cancelled out entirely, leaving the ion in a completely undamped oscillating state. Using a software

control loop interfaced to the acquisition system of the FPGA, this feedback gain is constantly controlled to maintain the undamped state. With this technique, the axial motion of the ion was successfully held at a constant amplitude for an arbitrary amount of time.
Various measurements for the characterization of the feedback system in connection with the detection electronics of the PENTATRAP experiment were carried out. A measurement of the resonator characteristics for a broad range of different feedback parameters showed a close correlation to the mathematical model of resonator feedback, except for a phase deviation of $\approx 100°$. This can be attributed to previously unknown phase shifts within the detection electronics of the PENTATRAP experiment. The results of this measurement showed the capabilities of the feedback system to shift the resonance frequency of the resonator by several linewidths as well as to modify its quality factor Q by up to two orders of magnitude. By specifically applying feedback at a phase of 90° to the resonator, the apparent temperature of the ion detection system was successfully cooled below the 4.2 K environment of the cryogenic Penning-trap setup. In the future, this will be used to actively cool the temperature of the ion's axial motion, resulting in a lower phase noise and therefore opening up the possibility for frequency determinations with higher precision and lower systematic errors.
By using the special case of 180° feedback, the center frequency of the resonator can be shifted away from the axial eigenfrequency of the ion, resulting in a significant reduction of the ion damping. A shift of ≈2.8 kHz resulted in such a low damping, that an excited ion was visible as a peak in the frequency spectrum for several minutes. This result allowed the implementation of a new phase-sensitive measurement technique for the detection of the axial ion frequency at the PENTATRAP experiment. This technique, referred to as APnP, is similar to the conventional PnP technique, in that it uses the phase information of the ion to determine its frequency. As this technique is able to determine the axial frequency to a greater precision than the Fourier limit, it inherently has the potential to outperform the currently used single-dip method. The APnP technique was successfully tested for phase evolution times of 11 ms and 21 ms, resulting in phase uncertainties of 13° and 40°, respectively. Due to stability issues with the trapping potentials, resulting in a fluctuating axial frequency, it was not possible to achieve longer phase evolution times. However, after the stability issues are resolved, the APnP technique is expected to function with longer phase evolution times and therefore greatly improve the precision of the axial frequency determination. As the precision of the PENTATRAP experiment is currently mainly limited by the uncertainty of the axial frequency, this technique will directly contribute to improving the precision of the mass measurements.

Appendix A: Schematics

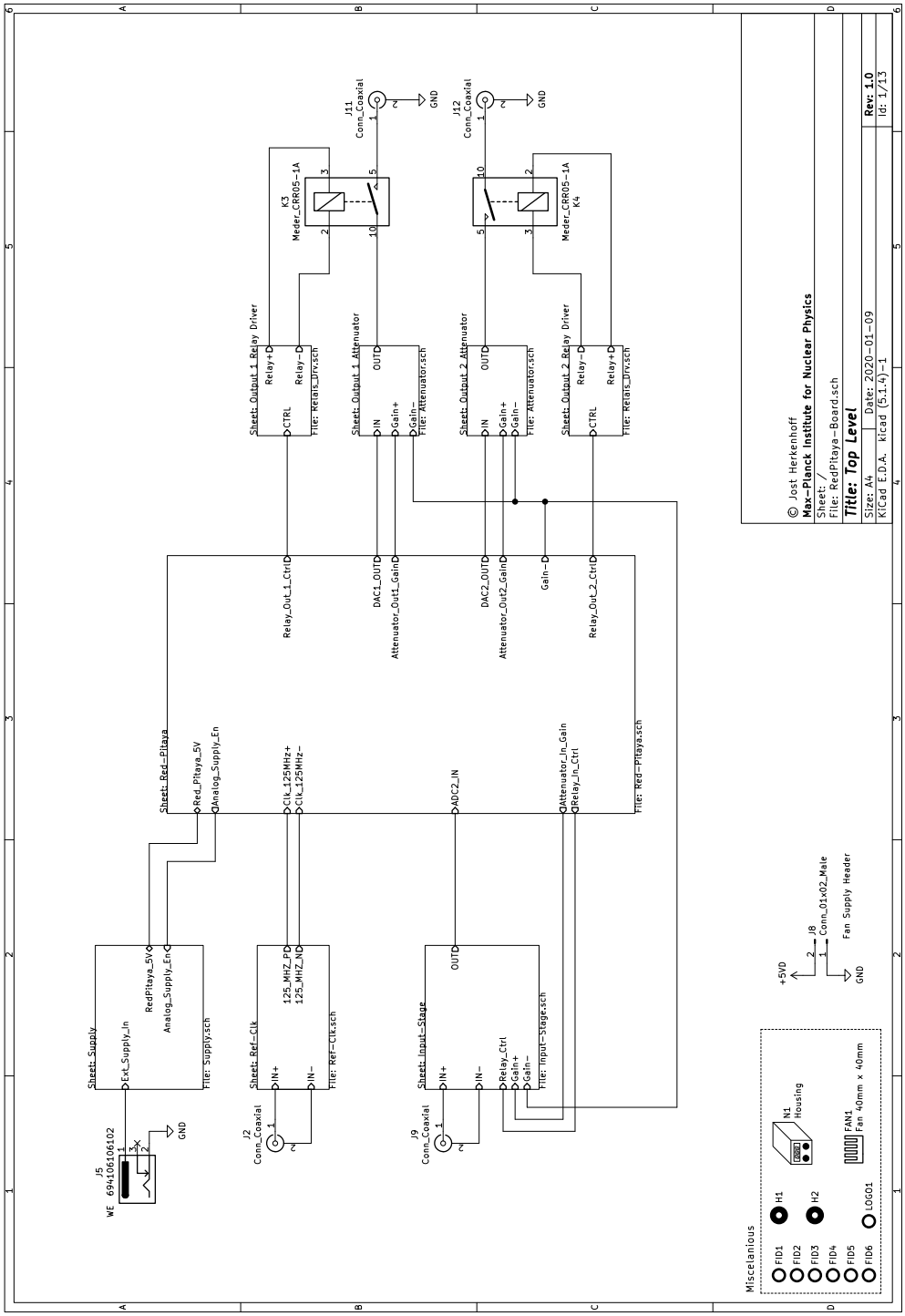

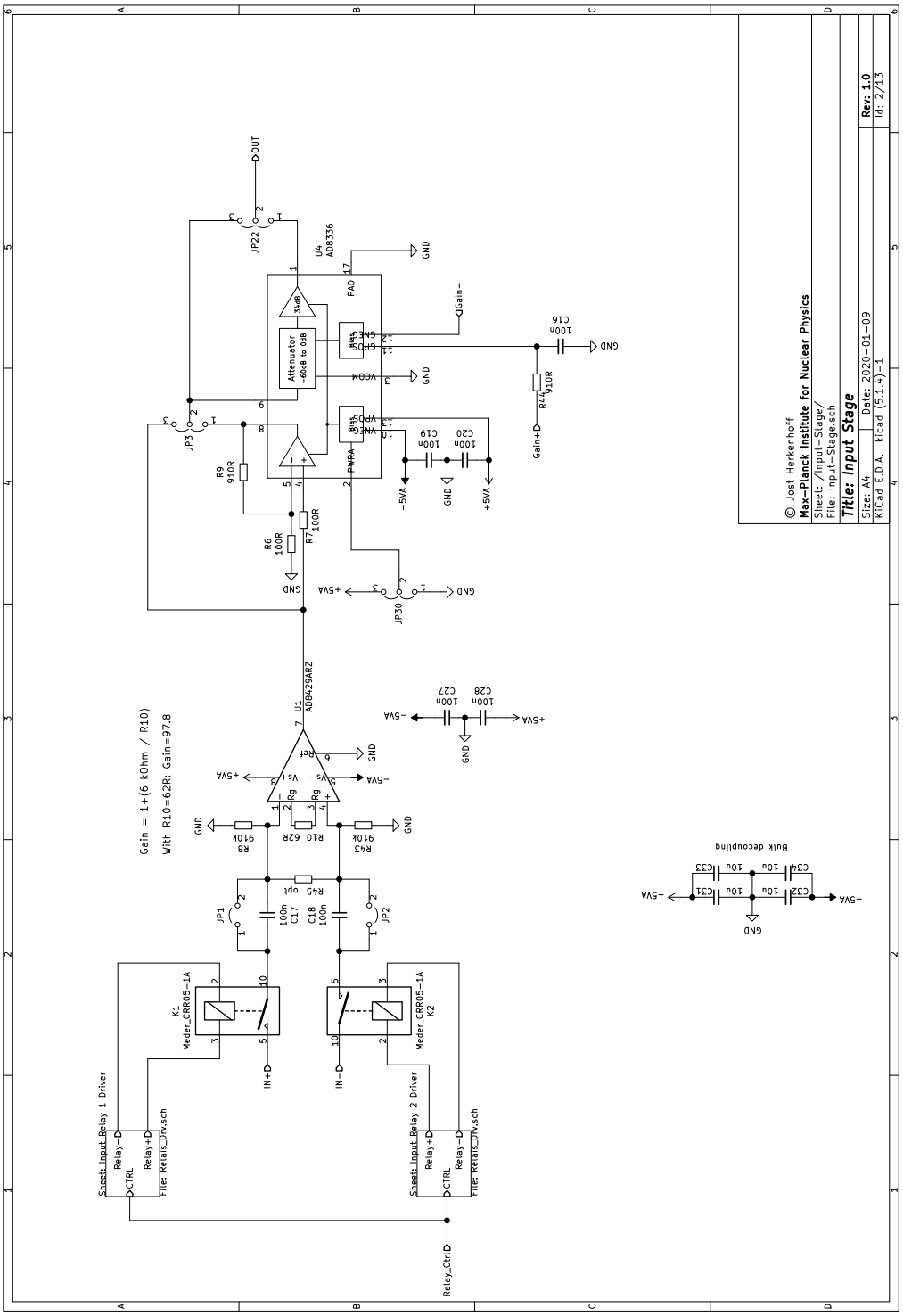
© Jost Herkenhoff
Max-Planck Institute for Nuclear Physics
Sheet: /Input-Stage/
File: Input-Stage.sch
Title: Input Stage
Size: A4
Date: 2020-01-09
Rev: 1.0
KiCad E.D.A. kicad (5.1.4)-1
Id: 2/13
Gain = 1+(6 kOhm / R10)
With R10=62R: Gain=97.8
Bulk decoupling
Sheet: Input Relay 1 Driver
Sheet: Input Relay 2 Driver
File: Relais_Drv.sch
Relay_Ctrl
IN+
IN-
Gain+
Gain-
OUT
GND
+5VA
-5VA
U1 AD8429ARZ
U4 AD8336
K1 Meder_CRR05-1A
K2 Meder_CRR05-1A
JP1
JP2
JP3
JP22
JP30
R4 910R
R5 opt
R6 100R
R7 100R
R9 910R
R10 62R
R43 910k
R8 910k
C16 100n
C17 100n
C18 100n
C19 100n
C20 100n
C27 100n
C28 100n
C31 10u
C32 10u
C33 10u
C34 10u

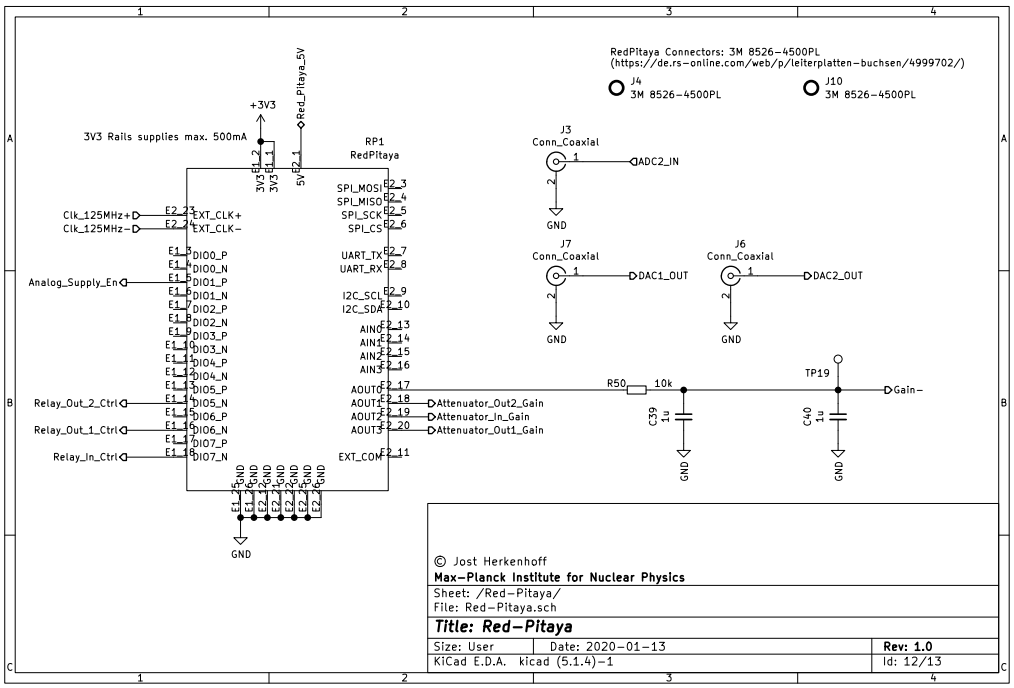
RedPitaya Connectors: 3M 8526-4500PL
(https://de.rs-online.com/web/p/leiterplatten-buchsen/4999702/)
J4
3M 8526-4500PL
J10
3M 8526-4500PL
+3V3
Red_Pitaya_5V
3V3 Rails supplies max. 500mA
RP1
RedPitaya
J3
Conn_Coaxial
ADC2_IN
GND
J7
Conn_Coaxial
DAC1_OUT
J6
Conn_Coaxial
DAC2_OUT
Clk_125MHz+
Clk_125MHz-
EXT_CLK+
EXT_CLK-
SPI_MOSI
SPI_MISO
SPI_SCK
SPI_CS
UART_TX
UART_RX
I2C_SCL
I2C_SDA
AIN0
AIN1
AIN2
AIN3
AOUT0
AOUT1
AOUT2
AOUT3
EXT_COM
Analog_Supply_En
Relay_Out_2_Ctrl
Relay_Out_1_Ctrl
Relay_In_Ctrl
Attenuator_Out2_Gain
Attenuator_In_Gain
Attenuator_Out1_Gain
R50
10k
C39
1u
C40
1u
TP19
Gain-
© Jost Herkenhoff
Max-Planck Institute for Nuclear Physics
Sheet: /Red-Pitaya/
File: Red-Pitaya.sch
Title: Red-Pitaya
Size: User
Date: 2020-01-13
Rev: 1.0
KiCad E.D.A. kicad (5.1.4)-1
Id: 12/13

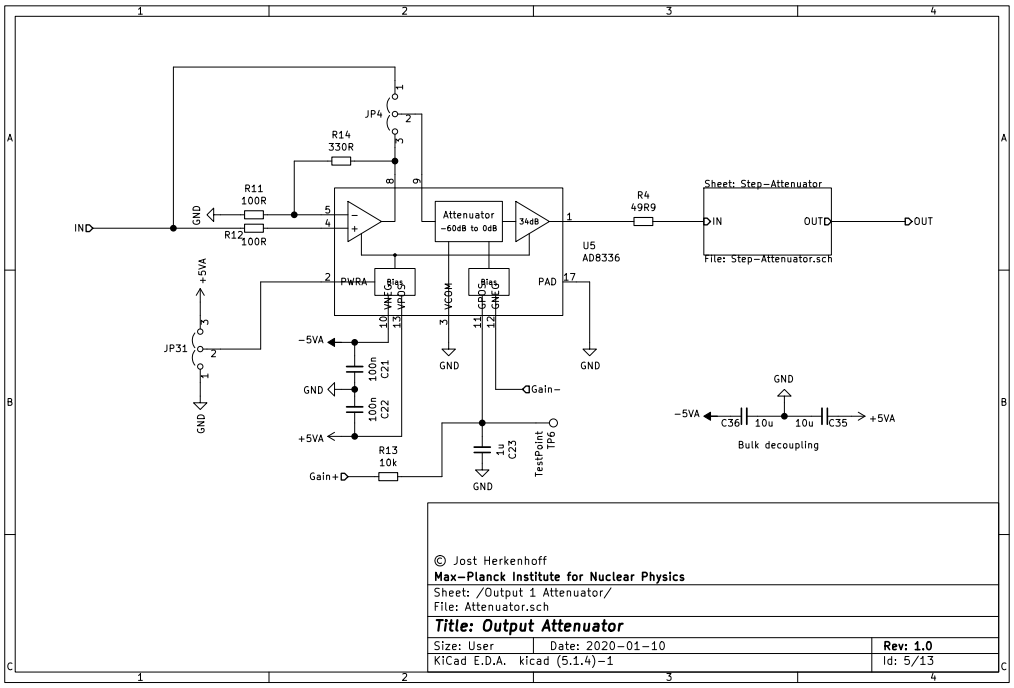
JP4
R14
330R
R11
100R
R12
100R
IN
GND
Attenuator
-60dB to 0dB
34dB
R4
49R9
Sheet: Step-Attenuator
IN
OUT
File: Step-Attenuator.sch
U5
AD8336
PWRA
PAD
+5VA
-5VA
JP31
100n
C21
100n
C22
Gain-
Gain+
R13
10k
1u
C23
TestPoint
TP6
Bulk decoupling
C36
10u
10u
C35
© Jost Herkenhoff
Max-Planck Institute for Nuclear Physics
Sheet: /Output 1 Attenuator/
File: Attenuator.sch
Title: Output Attenuator
Size: User
Date: 2020-01-10
Rev: 1.0
KiCad E.D.A. kicad (5.1.4)-1
Id: 5/13

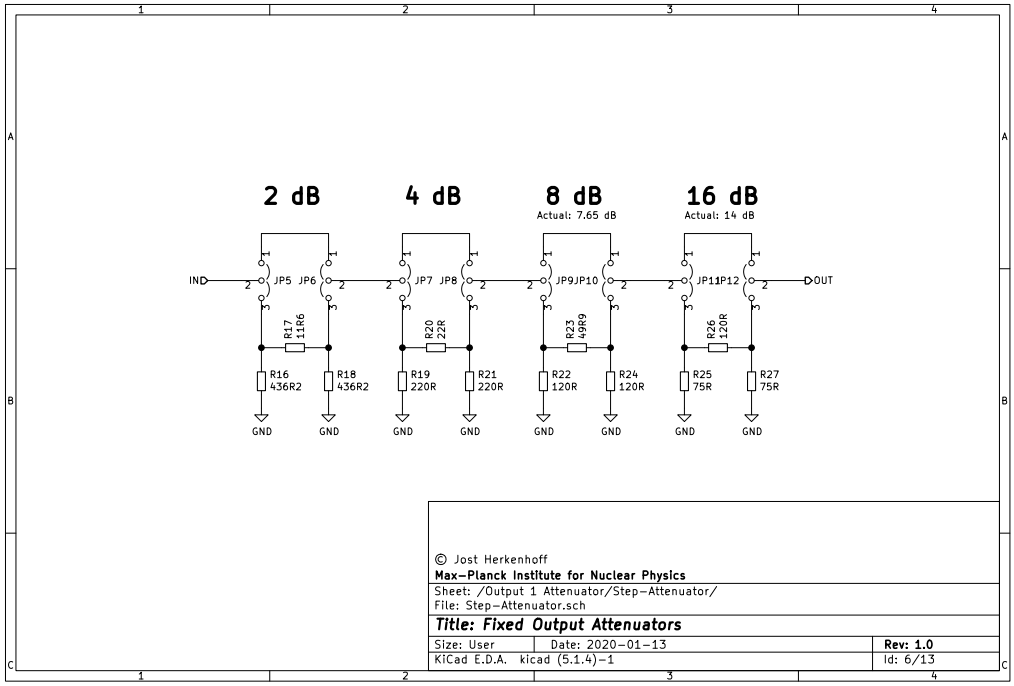
2 dB
4 dB
8 dB
Actual: 7.65 dB
16 dB
Actual: 14 dB
IN
OUT
JP5 JP6
JP7 JP8
JP9JP10
JP11P12
R17 1146
R20 22R
R23 4969
R26 120R
R16 436R2
R18 436R2
R19 220R
R21 220R
R22 120R
R24 120R
R25 75R
R27 75R
GND
© Jost Herkenhoff
Max-Planck Institute for Nuclear Physics
Sheet: /Output 1 Attenuator/Step-Attenuator/
File: Step-Attenuator.sch
Title: Fixed Output Attenuators
Size: User
Date: 2020-01-13
Rev: 1.0
KiCad E.D.A. kicad (5.1.4)-1
Id: 6/13

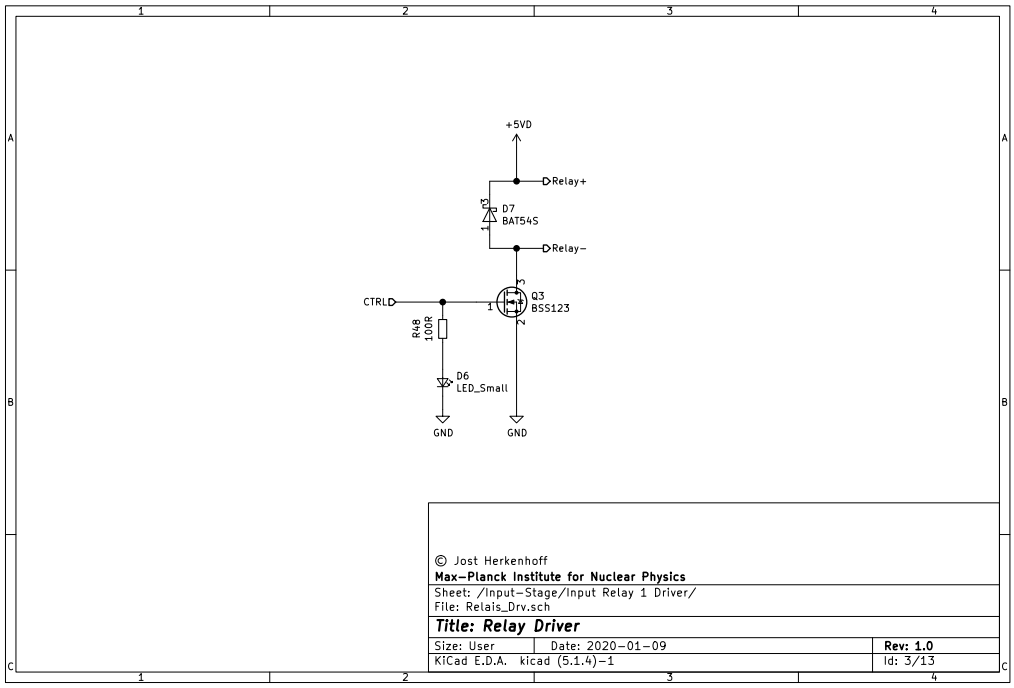
+5VD
Relay+
D7
BAT54S
Relay-
CTRLD
Q3
BSS123
R48
100R
D6
LED_Small
GND
© Jost Herkenhoff
Max-Planck Institute for Nuclear Physics
Sheet: /Input-Stage/Input Relay 1 Driver/
File: Relais_Drv.sch
Title: Relay Driver
Size: User
Date: 2020-01-09
Rev: 1.0
KiCad E.D.A. kicad (5.1.4)-1
Id: 3/13

5V Digital Rail

Part	Current each	Count	Current total
Relay	33 mA	4	133 mA
Fan	120 mA	1	120 mA
		Total:	153 mA

3V3 Digital Rail

Part	Current each	Count	Current total
AD9552	169 mA	1	169 mA
LTC6957	19 mA	1	19 mA
		Total:	188 mA

+/− 5V Analog Rail

Part	Current each	Count	Current total	
AD8429	10 mA	1	10 mA	
AD8336	30 mA	3	90 mA	Quiescent Current
AD8336	20 mA	2	40 mA	50 Ohm Load current
		Total:	140 mA	

While the LDOs low dropout voltage of around 300 mV allows for low power dissipation, their PSSR is better at higher Input-to-Output differential voltages.
The LT3045 datasheet shows a sweet spot at around 3 V.

The power dissipation in the LDO can be calculated using the following equation:
P = I_Out * (V_In − V_Out) + I_GND * V_In
Assuming a worst case output current of 200 mA and a dropout voltage of 3 V, the power dissipation is about 0.65 W. (I_GND is approximately 6 mA at 200 mA output current)

Assuming a Thermal resistance of 35°C/W for the MSOP package with a small copper area heatsink (see datasheet), the junction temperature rise above ambient approximately equals: 23°C
This is well within specs (T_junction_max = 120°C) for "normal" ambient temperatures

Input selection & protection

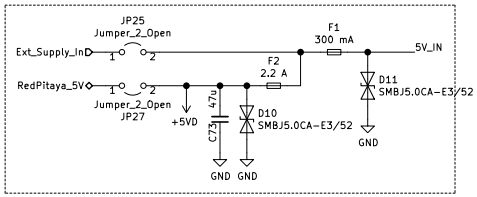

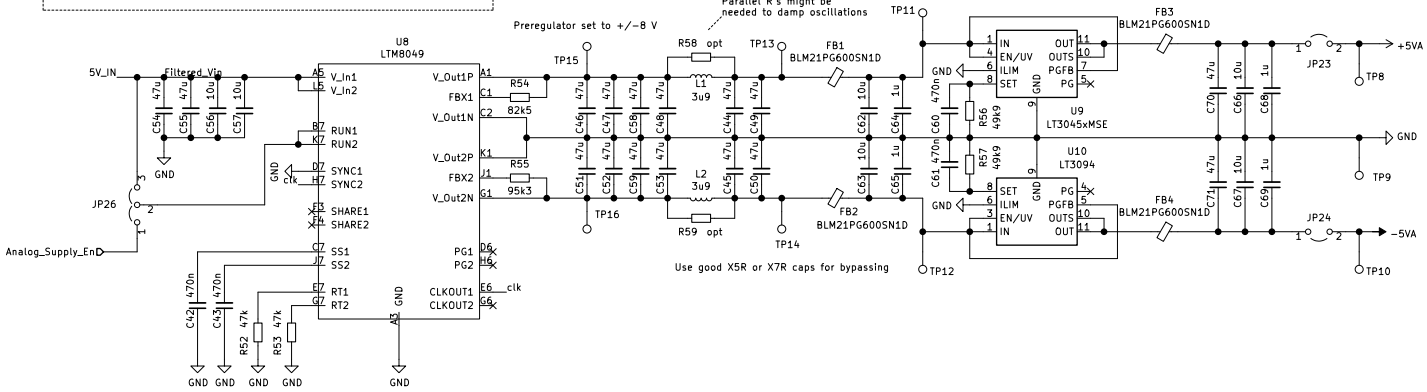

Switching frequency of LTM8049 is set using the resistors on RT1 and RT2 Pins (R52, R53).
R = (81.6 / f) − 1 (R in kOhm, f in MHz)

Switching frequency recommendations for V_In=5V and V_Out=+/−8V
f (optimal): 1 MHz
f (max): 2.5 MHz

Since we do not want any switching noise in the 100 kHz to 1 MHz range, a frequency of 1.7 MHz was chosen. This leads to tradeoffs in efficiency and max current capabilities, but that shouldnt be a problem here...

Max-Planck Institute for Nuclear Physics

Sheet: /Supply/
File: Supply.sch

Title: Power Supply

Size: A4	Date: 2020-01-13	**Rev: 1.0**
KiCad E.D.A. kicad (5.1.4)-1		Id: 11/13

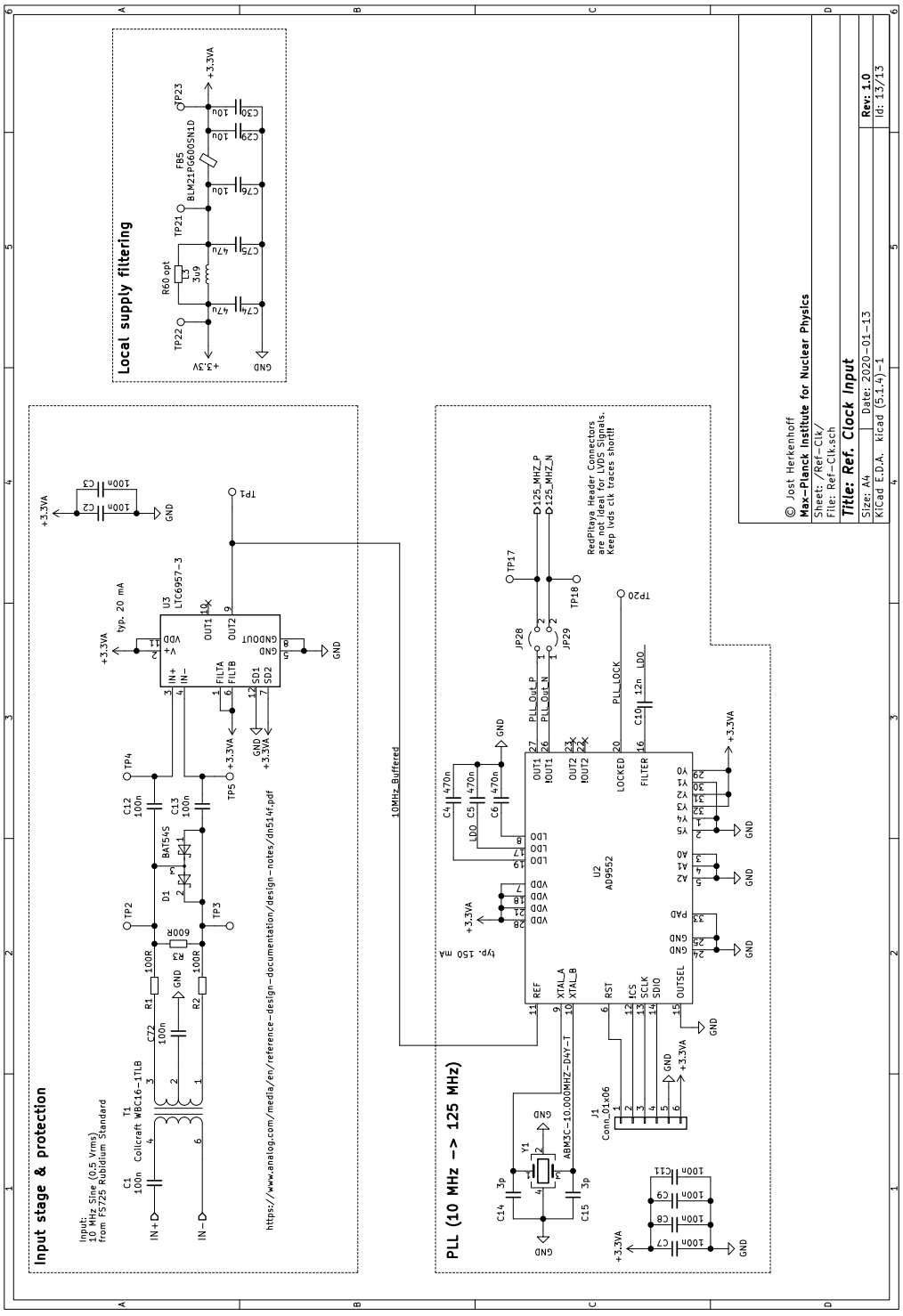
Input stage & protection
PLL (10 MHz -> 125 MHz)
Local supply filtering
10MHz_Buffered
125_MHZ_P
125_MHZ_N
RedPitaya Header Connectors are not all for VCC signals. Keep lvds clk traces short!!
https://www.analog.com/media/en/reference-design-documentation/design-notes/dn514f.pdf
© Jost Herkenhoff
Max-Planck Institute for Nuclear Physics
Sheet: /Ref-Clk/
File: Ref-Clk.sch
Title: Ref. Clock Input
Size: A4
Date: 2020-01-13
Rev: 1.0
KiCad E.D.A. kicad (5.1.4)-1
Id: 13/13

Appendix B: PCB Layout

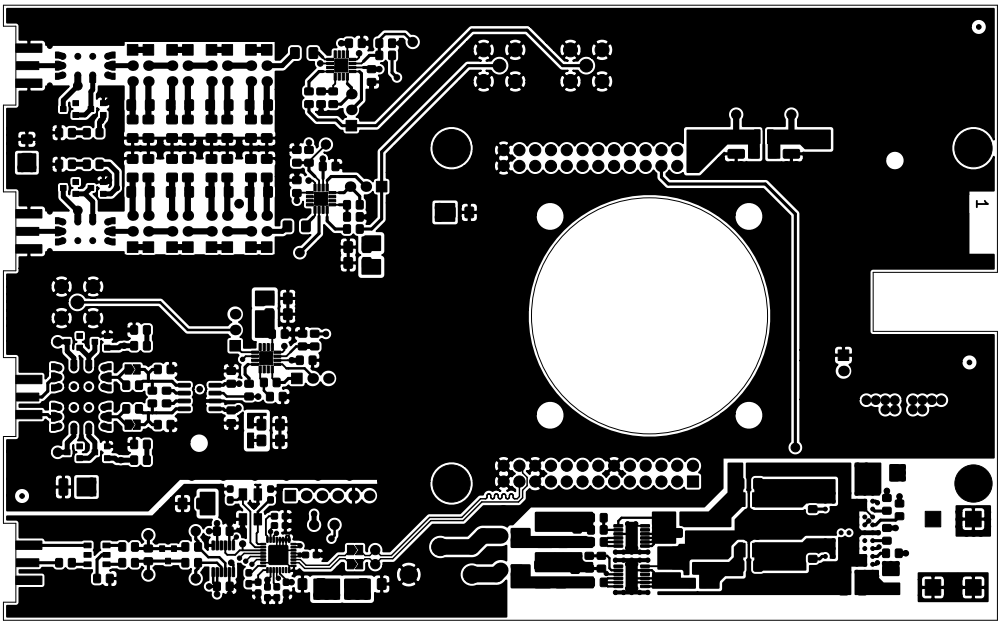

Figure B.1: PCB layout - Top layer

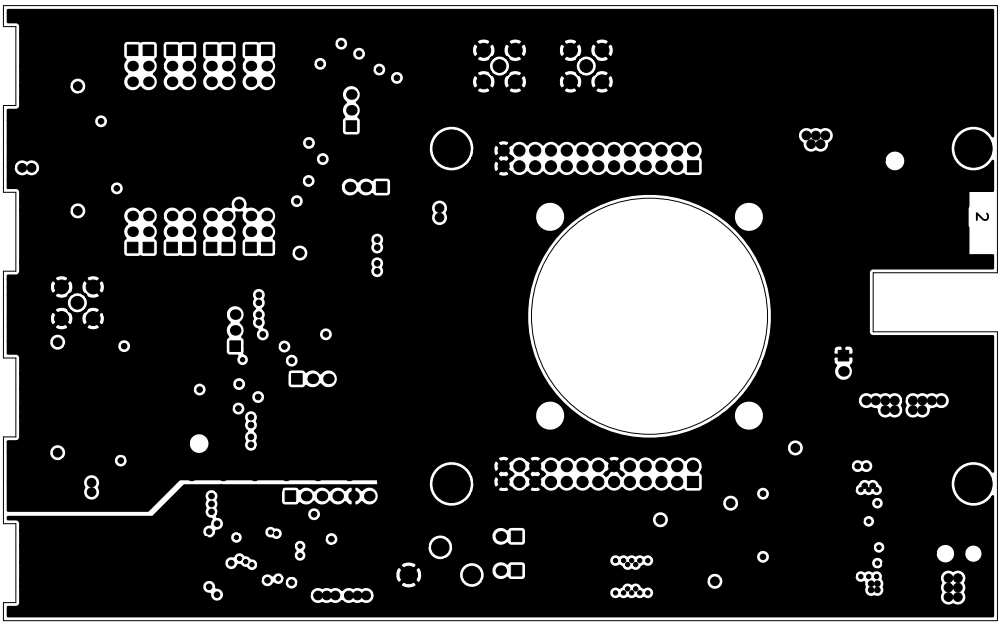

Figure B.2: PCB layout - Inner layer 1 (Ground plane)

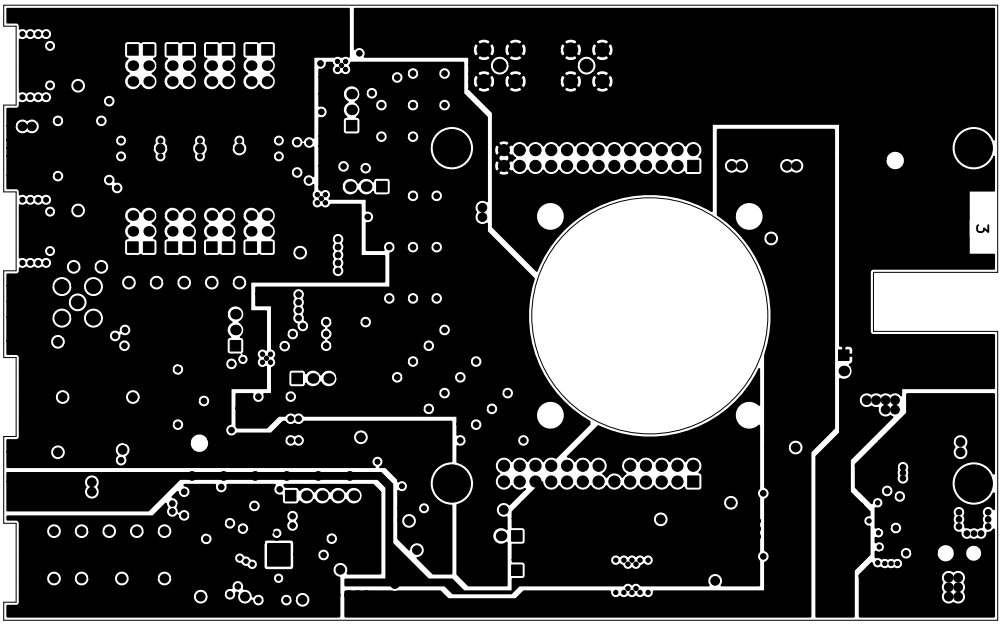

Figure B.3: PCB layout - Inner layer 2 (Supply planes)

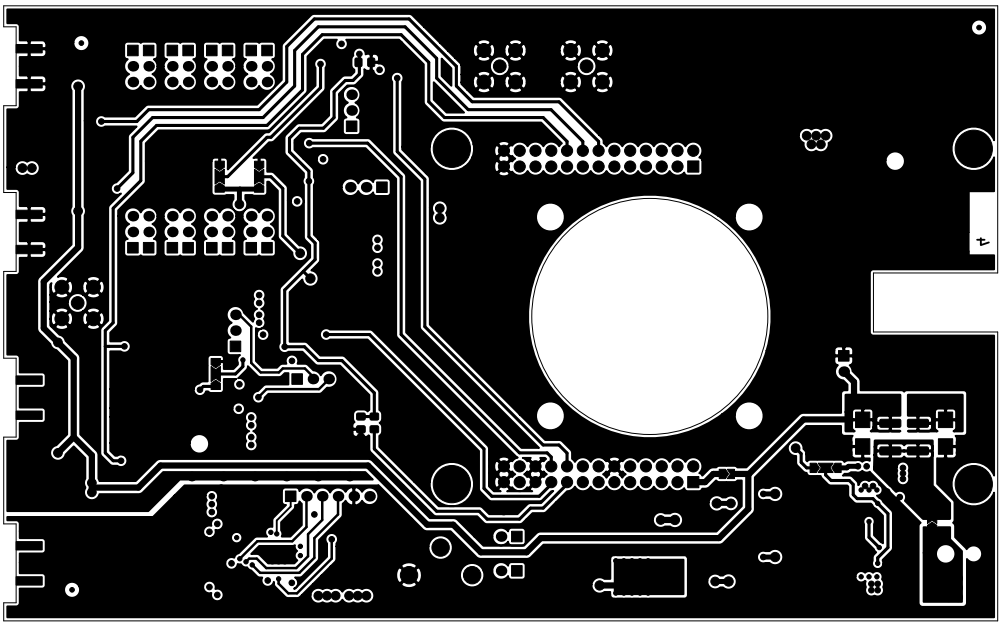

Figure B.4: PCB layout - Bottom layer

Bibliography

[1] B. Fogelberg et al. "Precise Atomic Mass Values near S132n: The Resolution of a Puzzle". *Physical Review Letters* **82**.9 (1999), 1823–1826 (cited on page 1).

[2] I. Arapoglou et al. "g Factor of Boronlike Argon Ar40 13+". *Physical Review Letters* **122**.25 (2019) (cited on page 1).

[3] A. V. Volotka, D. A. Glazov, G. Plunien, and V. M. Shabaev. "Progress in quantum electrodynamics theory of highly charged ions". *Annalen der Physik* **525**.8-9 (2013), 636–646 (cited on page 1).

[4] G. Gabrielse et al. "Precision Mass Spectroscopy of the Antiproton and Proton Using Simultaneously Trapped Particles". *Physical Review Letters* **82**.16 (1999), 3198–3201 (cited on page 1).

[5] G. L. Greene, M. S. Dewey, E. G. Kessler, and E. Fischbach. "Test of special relativity by a determination of the Lorentz limiting velocity: Does $E = mc^2$?" *Physical Review D* **44**.8 (1991), R2216–R2219 (cited on page 1).

[6] S. Rainville et al. "A direct test of $E = mc^2$". *Nature* **438**.7071 (2005), 1096–1097 (cited on page 1).

[7] J. Dilling, K. Blaum, M. Brodeur, and S. Eliseev. "Penning-Trap Mass Measurements in Atomic and Nuclear Physics". *Annual Review of Nuclear and Particle Science* **68**.1 (2018), 45–74 (cited on page 1).

[8] S. Rainville. "An Ion Balance for Ultra-High-Precision Atomic Mass Measurements". *Science* **303**.5656 (2004), 334–338 (cited on page 1).

[9] R. S. V. Dyck et al. "Ultraprecise Atomic Mass Measurement of the alpha Particle and He 4". *Physical Review Letters* **92**.22 (2004) (cited on page 1).

[10] M. Redshaw, J. McDaniel, and E. G. Myers. "Dipole Moment of PH+ and the Atomic Masses of Si28, P31 by Comparing Cyclotron Frequencies of Two Ions Simultaneously Trapped in a Penning Trap". *Physical Review Letters* **100**.9 (2008) (cited on page 1).

[11] A. Dörr. "PENTATRAP:A novel Penning-trap systemfor high-precision mass measurements". PhD thesis. Ruprecht-Karls Universität, Heidelberg, 2015 (cited on pages 1, 8, 22).

[12] K. Blaum, Y. N. Novikov, and G. Werth. "Penning traps as a versatile tool for precise experiments in fundamental physics". *Contemporary Physics, 51: 2, 149 – 175 (2010)* (2009) (cited on pages 1–3).

[13] S. Eliseev et al. "Resonant Enhancement of Neutrinoless Double-Electron Capture in Gd152". *Physical Review Letters* **106**.5 (2011) (cited on page 1).

[14] L. Gastaldo et al. "The electron capture in 163Ho experiment ECHo". *The European Physical Journal Special Topics* **226**.8 (2017), 1623–1694 (cited on page 1).

[15] J. Repp et al. "PENTATRAP: a novel cryogenic multi-Penning-trap experiment for high-precision mass measurements on highly charged ions". *Applied Physics B* **107**.4 (2012), 983–996 (cited on pages 1, 20, 21).

[16] S. Earnshaw. "On the Nature of the Molecular Forces which Regulate the Constitution of the Luminiferous Ether". *Transactions of the Cambridge Philosophical Society* **7** (1848), 97 (cited on page 3).

[17] K. Blaum. "High-accuracy mass spectrometry with stored ions". *Physics Reports* **425**.1 (2006), 1–78 (cited on page 3).

[18] J. I. Cirac and P. Zoller. "Quantum Computations with Cold Trapped Ions". *Physical Review Letters* **74**.20 (1995), 4091–4094 (cited on page 3).

[19] L. S. Brown and G. Gabrielse. "Geonium theory: Physics of a single electron or ion in a Penning trap". *Reviews of Modern Physics* **58**.1 (1986), 233–311 (cited on pages 3, 4, 6).

[20] G. Gabrielse and F. Mackintosh. "Cylindrical Penning traps with orthogonalized anharmonicity compensation". *International Journal of Mass Spectrometry and Ion Processes* **57**.1 (1984), 1–17 (cited on page 4).

[21] R. Schuessler. "First High-Precision Mass Measurements at PENTATRAP on highly charged Xe and Re ions". PhD thesis. Ruprecht-Karls-Universität, Heidelberg, 2019 (cited on pages 7, 13, 20, 22).

[22] M. Kretzschmar. "A quantum mechanical model of Rabi oscillations between two interacting harmonic oscillator modes and the interconversion of modes in a Penning trap". *AIP Conference Proceedings 457*. AIP, 1999 (cited on page 8).

[23] A. G. Marshall, C. L. Hendrickson, and G. S. Jackson. "Fourier transform ion cyclotron resonance mass spectrometry: A primer". *Mass Spectrometry Reviews* **17**.1 (1998), 1–35 (cited on page 8).

[24] W. Shockley. "Currents to Conductors Induced by a Moving Point Charge". *Journal of Applied Physics* **9**.10 (1938), 635–636 (cited on page 8).

[25] S. Ramo. "Currents Induced by Electron Motion". *Proceedings of the IRE* **27**.9 (1939), 584–585 (cited on page 8).

[26] S. Ulmer. "First Observation of Spin Flips with a single Proton stored in a cryogenic Penning trap". PhD thesis. Heidelberg University, 2011 (cited on page 8).

[27] U. Bakshi and A. Bakshi. "Electric Circuits". Technical Publications, 2008 (cited on page 9).

[28] M. P. Bradley. "A sub-ppb measurement of the mass of cesium for a new determination of the fine-structure constant". PhD thesis. Massachusetts Institute of Technology., 2000 (cited on pages 10, 40).

[29] J. B. Johnson. "Thermal Agitation of Electricity in Conductors". *Physical Review* **32**.1 (1928), 97–109 (cited on pages 10, 14).

[30] H. Nyquist. "Thermal Agitation of Electric Charge in Conductors". *Physical Review* **32**.1 (1928), 110–113 (cited on pages 10, 14).

[31] M. S. Ebrahimi et al. "Resistive cooling of highly charged ions in a Penning trap to a fluid-like state". *Phys. Rev. A 98, 023423 (2018)* (2018) (cited on page 10).

[32] X. Feng et al. "Tank circuit model applied to particles in a Penning trap". *Journal of Applied Physics* **79**.1 (1996), 8–13 (cited on page 11).

[33] G. J. Ketter. "Theoretical treatment ofmiscellaneous frequency-shifts in Penning traps with classical perturbation theory". PhD thesis. Ruperto-Carola-University of Heidelberg, 2015 (cited on pages 12, 41).

[34] E. A. Cornell et al. "Single-ion cyclotron resonance measurement of M (CO +)/ M (N 2 +)". *Physical Review Letters* **63**.16 (1989), 1674–1677 (cited on page 13).

[35] S. Sturm. "The g-factor of the electron bound in 28Si13+: The most stringent test of bound-state quantum electrodynamics". PhD thesis. Johannes-Gutenberg Universität, Mainz, 2012 (cited on page 15).

[36] R. L. Forward. "Electronic cooling of resonant gravity gradiometers". *Journal of Applied Physics* **50**.1 (1979), 1–6 (cited on page 15).

[37] M. Levine et al. "The use of an electron beam ion trap in the study of highly charged ions". *Nuclear Instruments and Methods in Physics Research Section B: Beam Interactions with Materials and Atoms* **43**.3 (1989), 431–440 (cited on page 19).

[38] G. Zschornack et al. "DRESDEN ELECTRON BEAM ION SOURCES: LATEST DEVELOPMENTS" (2010) (cited on page 19).

[39] C. Schweiger et al. "Production of highly charged ions of rare species by laser-induced desorption inside an electron beam ion trap". *Review of Scientific Instruments* (2019) (cited on page 19).

[40] U. Kentsch et al. "Dresden EBIT: Results and perspectives". *Review of Scientific Instruments* **73**.2 (2002), 660–662 (cited on page 19).

[41] A. Rischka. "The First Direct QEC Measurement in 163Ho and the Development of the High-Precision Mass Spectrometer PENTATRAP for Neutrino Physics". PhD thesis. Ruperto-Carola-University of Heidelberg, 2018 (cited on pages 20, 22, 37).

[42] K. Kromer. "Environmentally-induced systematic effects at the high-precision mass spectrometer PENTATRAP". MA thesis. Ruprecht-Karls-Universität, Heidelberg, 2019 (cited on page 20).

[43] C.-E. Roux. "High-resolution mass spectrometry: The trap design and detection system of Pentatrap and new Q-values for neutrino studies". PhD thesis. Ruprecht-Karls Universität, Heidelberg, 2012 (cited on pages 21, 22).

[44] R. Schuessler. "A new Detection System for the high-precision Penning-trap mass spectrometer PENTATRAP". MA thesis. University of Heidelberg, 2015 (cited on page 22).

[45] N. Krishnamurthy, M. Mansour, and R. Cole. "Implementation challenges for feedback active noise cancellation". *Proc. Speech and Signal Processing (ICASSP) 2012 IEEE Int. Conf. Acoustics*. 2012, 1649–1652 (cited on page 25).

[46] "Red-Pitaya Website". https://www.redpitaya.com/. accessed: 2020 (cited on page 25).

[47] "Zynq-7000 SoC Data Sheet: Overview". v1.11.11. Xilinx. 2018 (cited on page 25).

[48] "LTC2145-14 Datasheet". Analog Devices. accessed: 2020 (cited on page 26).

[49] "DAC1401D125 Datasheet". Integrated Device Technology. accessed: 2020 (cited on page 26).

[50] "AD8336 Datasheet". Analog Devices. accessed: 2020 (cited on page 27).

[51] "FS725 Rubidium Frequency Standard Operation and Service Manual". 1.3. Stanford Research Systems. 2015 (cited on page 28).

[52] M. Azarian. "A robust 10MHz reference clock input protection circuit and distributor for RF systems". *Analog Circuit Design*. Elsevier, 2015, 1059–1060 (cited on page 28).

[53] "AD9552 Datasheet". Analog Devices. accessed: 2020 (cited on page 29).

[54] "LT3045 Datasheet". Analog Devices. accessed: 2020 (cited on page 30).

[55] "LT3094 Datasheet". Analog Devices. accessed: 2020 (cited on page 30).

[56] Xilinx. "UG761 - AXI Reference Guide". Xilinx. 2012 (cited on page 32).

[57] L. Cordesses. "Direct digital synthesis: a tool for periodic wave generation (part 1)". *IEEE Signal Processing Magazine* **21**.4 (2004), 50–54 (cited on page 32).

[58] P. Demin. "Red-Pitaya Notes". http://pavel-demin.github.io/red-pitaya-notes/. accessed: 2020 (cited on pages 33, 36).

[59] D. Hilbert. "Grundzüge einer allgemeinen Theorie der linearen Integralgleichungen". *Teubner-Archiv zur Mathematik*. Vieweg + Teubner Verlag, 1989, 8–171 (cited on page 34).

[60] E. Hogenauer. "An economical class of digital filters for decimation and interpolation". *IEEE Transactions on Acoustics, Speech, and Signal Processing* **29**.2 (1981), 155–162 (cited on page 36).

[61] "EPICS Website". https://epics-controls.org/about-epics/. accessed: 2020 (cited on page 37).

[62] M. Door. "New Controlsystem and first trap characterization measurements at the high-precision Penning-trap mass spectrometer Pentatrap". MA thesis. Ruprecht-Karls-Universität, Heidelberg, 2018 (cited on page 37).

[63] J. O. Smith. "Spectral Audio Signal Processing". accessed: 2020 (cited on page 38).

[64] G. Gabrielse. "Probing a Single Isolated Electron: New Measurements of the Electron Magnetic Moment and the Fine Structure Constant". *The Spin*. Birkhäuser Basel, 2009, 105–145 (cited on page 38).

[65] S. Stahl et al. "Phase-sensitive measurement of trapped particle motions". *Journal of Physics B: Atomic, Molecular and Optical Physics* **38**.3 (2005), 297–304 (cited on pages 40, 41).

[66] S. Cavassila et al. "Cramer-Rao bounds: an evaluation tool for quantitation". *NMR in Biomedicine* **14**.4 (2001), 278–283 (cited on page 41).

[67] S. Sturm, A. Wagner, B. Schabinger, and K. Blaum. "Phase-Sensitive Cyclotron Frequency Measurements at Ultralow Energies". *Physical Review Letters* **107**.14 (2011) (cited on page 41).

[68] D. Lange. "Untersuchung des Dip-Fit-Algorithmus zur Bestimmung der Axialfrequenz beim Hochpräzisions-Massenspektrometer PENTATRAP". MA thesis. Ruprecht-Karls-Universität, Heidelberg, 2019 (cited on page 44).

[69] C. Böhm et al. "An ultra-stable voltage source for precision Penning-trap experiments". *Nuclear Instruments and Methods in Physics Research Section A: Accelerators, Spectrometers, Detectors and Associated Equipment* **828** (2016), 125–131 (cited on page 51).

Erklärung

Ich versichere, dass ich diese Arbeit selbstständig verfasst und keine anderen als die angegebenen Quellen und Hilfsmittel benutzt habe.

Bremen, 09.03.2020, _____